END

MICROCOPY RESOLUTION TEST CHART

NATIONAL BUREAU OF STANDARDS 1963 A

AD-A148 904

# Hydrodynamic Response of a Radiating Aℓ Plasma Excited by a Proton Beam

J. E. ROGERSON, R. W. CLARK AND J. DAVIS

*Plasma Radiation Branch*
*Plasma Physics Division*

December 20, 1984

DTIC FILE COPY

**NAVAL RESEARCH LABORATORY**
Washington, D.C.

SELECTED
DEC 2 7 1984

A

84 12 17 049

AD-A148904

# REPORT DOCUMENTATION PAGE

| 1a REPORT SECURITY CLASSIFICATION | 1b RESTRICTIVE MARKINGS |
|---|---|
| UNCLASSIFIED | |
| 2a SECURITY CLASSIFICATION AUTHORITY | 3 DISTRIBUTION/AVAILABILITY OF REPORT |
| 2b DECLASSIFICATION/DOWNGRADING SCHEDULE | Approved for public release; distribution unlimited. |

| 4 PERFORMING ORGANIZATION REPORT NUMBER(S) | 5 MONITORING ORGANIZATION REPORT NUMBER(S) |
|---|---|
| NRL Memorandum Report 5482 | |

| 6a NAME OF PERFORMING ORGANIZATION | 6b OFFICE SYMBOL (If applicable) | 7a NAME OF MONITORING ORGANIZATION |
|---|---|---|
| Naval Research Laboratory | Code 4720 | Defense Nuclear Agency |

| 6c ADDRESS (City, State, and ZIP Code) | 7b ADDRESS (City, State, and ZIP Code) |
|---|---|
| Washington, DC 20375-5000 | Washington, DC 20305 |

DEC 27 1984

A

| 8a NAME OF FUNDING/SPONSORING ORGANIZATION | 8b OFFICE SYMBOL (If applicable) | 9. PROCUREMENT INSTRUMENT IDENTIFICATION NUMBER |
|---|---|---|
| Defense Nuclear Agency | RAEV | |

| 8c ADDRESS (City, State and ZIP Code) | 10 SOURCE OF FUNDING NUMBERS | | | |
|---|---|---|---|---|
| | PROGRAM ELEMENT NO | PROJECT NO | TASK NO | WORK UNIT ACCESSION NO |
| Washington, DC 20305 | 62715H | | | DN880-191 |

11 TITLE (Include Security Classification)

Hydrodynamic Response of a Radiating Aℓ Plasma Excited by a Proton Beam

12 PERSONAL AUTHOR(S)
Rogerson, J.E., Clark, R.W. and Davis, J.

| 13a TYPE OF REPORT | 13b TIME COVERED | | 14 DATE OF REPORT (Year, Month, Day) | 15 PAGE COUNT |
|---|---|---|---|---|
| Interim | FROM _____ | TO _____ | 1984 December 20 | 56 |

16 SUPPLEMENTARY NOTATION  This research was sponsored by the Defense Nuclear Agency, under Subtask T99QAXLA, work unit 00004 and work unit title "Advanced Simulation Concepts."

| 17 | COSATI CODES | | 18 SUBJECT TERMS (Continue on reverse if necessary and identify by block number) | |
|---|---|---|---|---|
| FIELD | GROUP | SUB-GROUP | Ion beam | Stopping power |
| | | | Plasma | Radiation transport |

19 ABSTRACT (Continue on reverse if necessary and identify by block number)

A fully self-consistent one-dimensional ion beam-slab interaction model has been developed which describes the slowing down of the beam, the hydrodynamic response and ionization dynamics of the slab, and detailed radiation emission and transport. An extensive atomic level structure with collisional radiative ionization dynamics is employed in conjunction with a hybrid radiation transport scheme which consists of a multi-frequency formalism for continuum transport and a probabilistic treatment for line transport. It is found that beam deposition and slab response depend strongly on radiation transport within the slab. Temperature and density profiles and emission spectra are presented.

| 20 DISTRIBUTION/AVAILABILITY OF ABSTRACT | | | 21. ABSTRACT SECURITY CLASSIFICATION |
|---|---|---|---|
| ☒ UNCLASSIFIED/UNLIMITED  ☐ SAME AS RPT  ☐ DTIC USERS | | | UNCLASSIFIED |
| 22a NAME OF RESPONSIBLE INDIVIDUAL | 22b TELEPHONE (Include Area Code) | | 22c OFFICE SYMBOL |
| J. Davis | (202) 767-3278 | | Code 4720 |

**DD FORM 1473, 84 MAR**    83 APR edition may be used until exhausted
All other editions are obsolete

SECURITY CLASSIFICATION OF THIS PAGE

i

# CONTENTS

A-1

iii

# HYDRODYNAMIC RESPONSE OF A RADIATING Aℓ PLASMA EXCITED BY A PROTON BEAM

## I. INTRODUCTION

Recent advances in pulsed power and diode technologies have made it possible to deliver intense proton beams onto a planar slab with high efficiency. For example, focussed proton beams with energy of the order of an MeV and with current densities of several kA/cm$^2$ have been reported.[1-3] Thus, the interaction of energetic charged particle beams with planar slab materials has become an active field of research. One significant application is the use of ion beams to generate x-rays for materials research, lethality and vulnerability studies.

The investigation of charged particle beam-matter interaction involves consideration of several phenomena. First, there is the energy deposition within the slab by the beam. Then, there is the subsequent hydrodynamic motion of the slab as it responds to this energy influx; a blow-off region develops on the front (beam) side of the plasma, while the back surface recoils away from the beam. As the slab plasma beats up, the plasma ions emit radiation which can affect the energy balance of the plasma. Thus at any instant in the plasma, there is the interplay of deposited beam energy, thermal conduction, hydrodynamic motion, radiation transport, plasma internal energy, magnetic fields, etc. to be taken into account.

With the exception of magnetic and electric field effects, this paper represents an attempt to treat all these effects self-consistently in a one-dimensional simulation of a proton beam incident on an initially solid density Aℓ slab.

## II. THEORETICAL MODEL

The interaction of the ion beam with the slab plasma is strongly dependent on the local temperature and degree of ionization in the slab. In addition, optical pumping and energy transport by photons of all frequencies can influence the plasma temperature and degree of ionization, and can modify the hydrodynamic response of the slab. Thus, the deposition of the beam, the hydrodynamic evolution and atomic physics of the slab, as well as the transport of radiation, must be calculated self-consistently.

Discussion of the theoretical model can be separated for convenience as follows: (a) hydrodynamics and thermal conduction (b) ionization and atomic physics (c) radiation emission and transport and (d) beam dynamics and energy deposition.

### (A) Hydrodynamics and Thermal Conduction

The basic hydrodynamic variables of mass, momentum, and total energy are transported in one dimension using a numerical scheme with a sliding-zone version of flux-corrected transport.[4] A special gridding algorithm is used which moves zones in a Lagrangian fashion and adjusts the mesh in order to resolve steep gradients in the flow. The hydrodynamic equations solved are

$$\frac{D\rho}{Dt} = \frac{\partial \rho}{\partial t} + \frac{\partial}{\partial x} (u\rho) = 0, \tag{1}$$

$$\frac{D(\rho u)}{Dt} = - \frac{dP}{dx}, \tag{2}$$

$$\frac{D\varepsilon_T}{Dt} = - \frac{\partial}{\partial x} (uP) + \dot{\varepsilon}_{rad} + \dot{\varepsilon}_{dep}$$

$$+ \frac{\partial}{\partial x} \left\{ \eta N \frac{\partial}{\partial x} T \right\}, \tag{3}$$

where $\rho$ is mass density, $u$ is velocity, $P$ is pressure, $\varepsilon_T$ is total energy density, $\dot{\varepsilon}_{rad}$ is the rate of energy loss or gain due to radiation, $\dot{\varepsilon}_{dep}$ is the rate of energy gain due to the beam deposition process, $\eta$ is the thermal conductivity, and $N$ is the ion density. The thermal conduction is calculated implicitly, using an iterative Crank-Nicholson scheme.

Since densities did not much exceed solid density in this study, a simple equation of state was assumed with

$$P = \frac{2}{3} (\varepsilon_T - \frac{1}{2} \rho u^2 - \varepsilon_I), \tag{4}$$

where $\varepsilon_I$ is the ion potential energy due to ionization and excitation. A single temperature model was employed,

2

$$kT = \frac{P}{(\rho/m_I)(1+\bar{Z})} , \qquad (5)$$

where $m_I$ is ion mass, and T is temperature. The ionization energy, $\varepsilon_I$, and effective charge, $\bar{Z}$ are calculated from the ionization-radiation equations which are explained below. A single temperature assumption is valid in the solid dense material as well as in the beam deposition region, since thermal equilibration times are short compared with the time scales of the energy input and changes in the hydrodynamic variables.

The local rate of change of energy due to radiation transport $\dot{\varepsilon}_{rad}$, and that due to the beam deposition $\dot{\varepsilon}_{dep}$, will be discussed in Sections C and D.

### (B) Ionization and Atomic Physics

The ionic populations in the plasma may be characterized by a set of atomic rate equations of the form

$$\frac{df_i}{dt} = \Sigma_j W_{ji} f_j - \Sigma_i W_{ij} f_i \qquad (6)$$

where $f_i$ is the fractional population of atomic level i, and $W_{ji}$ is the net reaction rate describing the transition from initial state j to final state i. An equation of this type is constructed for each of the atomic levels included in the model.

For sufficiently dense plasmas of the sort we expect to model with the ion-beam code, the effective populating and depopulating rates are generally fast compared with the hydrodynamic response. An equilibrium assumption can be justified, which involves dropping the explicit time dependence in equation (6). The plasma is then said to be in collisional-radiative equilibrium (CRE),[5] whereby the plasma ionization state responds instantaneously to changes in hydrodynamic quantities.

The rate coefficients that are used to calculate the populating and depopulating rates, $W_{ji}$, are calculated using various scattering techniques. The processes included in this calculation and the methods

used in calculating the corresponding rate coefficients are summarized below.

(1)  Collisional ionization - exchange classical impact-parameter (ECIP) methods[6] (the effect of autoionizing resonances on the cross sections has been ignored).

(2)  Photoionization - hydrogenic approximation with Karzas-Latter-Gaunt factors[7,8].

(3)  Dielectronic recombination - the detailed calculations of Jacobs et al.[9] are used.

(4)  Collisional excitation  - Coulomb-Born distorted-wave approximation including exchange effects[10], or the semiclassical impact-parameter (SCI) technique[11].

(5)  Spontaneous radiative decay - oscillator strengths are taken from several calculations and measurements[12].

(6)  Photoexcitation - oscillator strengths used are those quoted above to determine optical depths (see the next section on radiation transport).

Finally, collisional and radiative recombination, collisional deexcitation, and stimulated emission are all calculated as the detailed balance of the corresponding opposite rate listed above.

Once the set of rate equations (including the radiation transport) has been solved for the level populations, $f_i$, the electron density can be calculated,

$$N_e = \sum_i z_i f_i N_I \tag{7}$$

where $z_i$ is the ionic charge of level i and $N_I$ is the total ion density.

4

The ionization and excitation energy can also be calculated by

$$\varepsilon_1 = \sum_i \chi_i f_i N_I,$$ (8)

where $\chi_i$ is the energy of level i, measured from the ground state of the neutral atom.

## (C) Radiation Emission and Transport

Radiation emission from a plasma and its opacity are dependent on the local atomic level population densities. Except for optically thin plasmas, however, the level populations depend on the radiation field, since optical pumping via photoionization and photoexcitation can produce significant population redistribution. Thus, the ionization and radiation transport processes are strongly coupled and must be solved self-consistently. In this model, an iterative procedure[13] is used, where level populations are calculated using the radiation field from the previous iteration, then using these populations to calculate a new radiation field and recalculating populations until convergence is reached.

Three distinct radiation transport schemes have been developed, and can be used interchangeably in the code: A probabilistic scheme, a multifrequency scheme and a hybrid method. Descriptions of these transport methods have appeared elsewhere; in this report, their general properties will be outlined.

The probabilistic model[14] forms local angle and frequency averaged escape probabilites for each emission line and for each bound-free process. Free-free radiation is treated with a multifrequency formalism. The radiation transport and emission spectra are calculated from these escape probabilities. The method is cost-effective, can treat comprehensive atomic models and provides good overall energetics, but cannot calculate certain spectral details and breaks down at very high densities.

The multifrequency model[15] solves the equation of radiation transport at a large number of discrete frequencies, providing resolution of emission lines, recombination edges and absorption edges. It provides accurate

5

radiation transport at high density, and gives spectral details such as self-absorption features. However, a large number of frequencies is required to provide adequate resolution, and it tends to be a relatively costly method.

The hybrid model uses the multifrequency formalism to transport the continuum (bound-free and free-free) radiation and frequency-integrated escape probabilities to transport the lines. Continuum opacities are interpolated from the multifrequency mesh and folded into the line transport calculations. The line opacities are assumed to have negligible impact on the continuum energetics.

In all of the models outlined above, local ionization state-dependent inner-shell opacities are included, since these processes are very important in the cool, dense plasma regions. Inner-shell photoionization cross sections for the neutral element are taken from the fits by Biggs and Lighthill,[16] and the positions of the ionization-dependent absorption edges are taken from the Hartree-Fock calculations of Clementi and Roetti.[17]

The local rate of energy change in zone j, due to radiation transport is given by

$$\varepsilon_j = - \sum_P (F_{Pj} - \sum_k C_{Pkj} F_{Pk}) \tag{9}$$

where $F_{Pk}$ is the rate of energy loss in zone k due to a discrete radiative process (or frequency group) P, and $C_{Pkj}$ is the radiative coupling of zone k to zone j for that process. The couplings are functions of opacity, integated over process and photon path. In the probabilistic model, a matrix of couplings must be computed for each bound-bound, bound-free and free-free process; for the multifrequency model, they must be computed for each discrete frequency. In this way, the net cooling and heating by radiation emission and absorption among the various zones of the plasma is accounted for accurately.

(D) Beam Dynamics and Energy Deposition

We assume that on the timescale of the slab response (several nanoseconds), the beam maintains uniform flow, that is

6

$$\rho_B u_B = \dot{m} = \frac{J \, m_B}{e \, Z_B} \qquad (10)$$

where $\rho_B$ and $u_B$ are the local mass density and axial velocity of the beam. The mass flux $\dot{m}$ is assumed constant up to the point the beam is stopped. $J$ is the beam current per unit area; $m_B$ and $Z_B$ are the mass and charge of a beam ion.

For a relativistic beam with negligible thermal spread, the kinetic energy of a beam ion is related to the local velocity by

$$E_B = \frac{m_B c^2}{\sqrt{(1-u_B^2/c)^2}} - m_B c^2 \; . \qquad (11)$$

The energy is also related to the stopping power by

$$E_B(x') = E_o - \int_{-\infty}^{x'} \left(\frac{dE}{dx}\right)_T dx \; , \qquad (12)$$

where $E_o$ is the initial energy, $x'$ is the distance into the slab, and the total stopping power is given by the sum of the ion-free electron, ion-bound electron and ion-plasma ion interactions,

$$\left(\frac{dE}{dx}\right)_T = \left(\frac{dE}{dx}\right)_e + \left(\frac{dE}{dx}\right)_b + \left(\frac{dE}{dx}\right)_i \; . \qquad (13)$$

## 1. Interaction With Bound Electrons

Two widely used models for calculating stopping cross sections are the LSS model, which is valid at low velocity, and the Bethe theory, which is valid at high velocity. These are complementary models and can be used to span the entire projectile velocity range [e.g., Mehlhorn[18]].

The chief difficulty in applying the Bethe theory is obtaining the mean excitation energy $\bar{I}$. The calculation of this quantity is a tedious exercise, and various scaling schemes have been proposed to estimate it [Mosher[19], Mehlhorn[18]). Also, alternate methods of calculating bound electron stopping power have been developed which do not involve this quantity. One of these is the local oscillator model [Rogerson[20], Nesbet

and Ziegler[21]]. This model involves an integral over the atomic (or ionic) electron density and thus depends on the accuracy of the electron distribution used in the calculations. For cold targets, a Thomas-Fermi density has been found to yield accurate stopping powers for cold target ions [Rogerson[20]].

In the local oscillator model (LOM)[20] representation of the stopping cross section, the spatial change of energy given by

$$\left(\frac{dE}{dx}\right)_b = (\rho(x)/m_I) \, S_b(V) \tag{14}$$

where $S_b(V)$ is the stopping cross section in erg-cm$^2$.

$$S_b(V) = \frac{4\pi Z_B^2 e^4}{mV^2} \int_0^R 4\pi \, r^2 \, \tilde{\rho}(r) \, K_o(\tau) \, dr, \tag{15}$$

where $Z_B$ is the effective charge of the projectile ion, R is the ion radius, e and m are the electron charge and mass, V is the projectile velocity, $\tilde{\rho}(r)$ is the local bound electron density in the target atom, and $K_o(\tau)$ is a modified zeroth order Bessel function.

$$\tau = \hbar \, \omega_o(r)/mV^2 \, , \tag{16}$$

where $\hbar$ is Planck's constant divided by $2\pi$, and $\omega_o(r)$ is the local plasma frequency at radius r within the atom.

There are three assumptions underlying the LOM[21]. The first is that a loss function can be defined, dependent only on the local electron density in the target atom. The second is that the longitudinal dielectric response can be represented by $\varepsilon(\omega)$ with a single zero at $\omega \sim \omega_o$, subject to the high frequency condition

$$\varepsilon(\omega) \sim 1 - \omega_o^2/\omega^2 \tag{17}$$

appropriate to free electrons. The third assumption is that the induced polarization charge is spread out from the ion trajectory to some finite radius of the order of the de Broglie wavelength $\hbar/mV$. This last

8

assumption is justified by the adiabatic argument that energy will be transferred only to electrons with velocity less than V. A wave packet with momentum of order mV would have a spatial spread of order $\hbar/mV$.

The electron density $\tilde{\rho}(r)$ is taken from the Thomas-Fermi (TF) model proposed by Zink.[22]

In a plasma target, the bound atomic electrons can be screened from the projectile ions by the free electrons. Thus, the LOM must be modified to take this shielding effect into account. For an electron in an isolated atom, the maximum impact parameter is $V/\omega$, where $\omega$ is a characteristic frequency of motion[23]. Plasma screening limits this parameter to the Debye length D. The expression for $\tau$ can be rewritten

$$\tau = (\hbar/mV)\ (\omega_o(r)/V). \tag{18}$$

Whenever $V/\omega_o(r) > D$, $\tau$ is taken to be

$$\tau = \hbar/mVD \tag{19}$$

Thus, plasma shielding of the bound electrons is taken into account by limiting the argument of the Bessel function.

Some criticism of the use of free-electron-gas approximations for bound electron stopping power (which includes the LOM) have been expressed[24]; it is argued that the use of a free electron gas model to calculate the Bethe mean excitation energy parameter $I(Z,q)$ — where Z is the nuclear charge, and q is the ionic charge-yields the wrong Z-scaling for hydrogenic ions; i.e., this model yields

$$I(Z,Z-1) = Z^{3/2}\ I(1,0)$$

instead of the correct

$$I(Z,Z-1) = Z^2\ I(1,0).$$

Comparison of $I(Z,q)$ for Al derived from the free-electron-gas approximation with $I(Z,q)$ derived from detailed calculation of Al electron power

for protons[25] show an increasing divergence with increasing q, with the free-electron-gas $I(Z,q)$ being lower.

Recently, McGuire, Peek, and Pitchford[25] (MPP) published detailed calculations of stopping power cross sections of protons by Aℓ ions. By using the generalized-oscillator-strength formulation of the Born approximation, they calculated tables of stopping cross sections for protons interacting with Aℓ ions of charge q, where $0 < q < 11$, in the energy range 0.1 MeV to 100 MeV.

The MPP cross sections for neutral Aℓ agreed very well with local oscillator model calculations[20], but for ionized Aℓ, the MPP cross sections were generally lower, (especially at lower energies) than the local-oscillator-model predictions. Figures 1 and 2 show comparisons of these cross sections for $Al^{+1}$ and $Al^{+5}$; these figures indicate generally the relative comparisons of the two sets of cross sections.

By use of least-squares methods, these MPP data were fitted by a function of the form

$$F_q(y) = \exp (A_q + B_q y + C_q y^2 + D_q y^3) , \qquad (20)$$

where $y = \ln (E/E_o)$, and $E_o = 0.1$ MeV. $F_q(y)$ gives stopping cross sections in units of $10^{-15}$ eV cm$^2$/atom. Table 1 gives the fitting parameters $A_q$, $B_q$, $C_q$ and $D_q$ for each value of q. Table 2 gives the MPP data and the results of Eq. (20). All the fits were within 7%, except for q=3, where the maximum deviation was 9%. Thus, Eq. (20) yielded good fits to the calculated cross section.

In the treatment of the beam-target interaction, the average ionic charge $\bar{Z}$ in a given cell is used to obtain stopping power. For non-integer values of $\bar{Z}$, Eq. (20) is used for q and q+1, where q is the integer part of $\bar{Z}$, and the stopping cross section for $\bar{Z}$ is obtained by linear interpolation between $F_q(y)$ and $F_{q+1}(y)$.

For q=0, q=1 and q=2, the MPP data, and hence the fits, are monotonically decreasing for energies $\geq 0.1$ MeV. For these cases, a local-oscillator model (LOM)[20] is used to calculate bound electron stopping power for energies below 0.1 MeV. These LOM cross sections are adjusted to match

10

the MPP data at 0.1 MeV, and the cross sections at lower energy are scaled accordingly. The MPP data for q = 8, 9, and 10 are also monotically decreasing for E ≥ 0.1 MeV, but at these charge levels, the stopping power is dominated by the free-electron contribution; hence, no adjustments to the bound electron stopping power at energies less than 0.1 MeV are made. The fits are just extended below 0.1 MeV.

For the other q values between 3 and 11, the MPP data peak in the 0.1 MeV – 100 MeV range; hence the fits are extended below 0.1 MeV to obtain low energy cross section data. For q > 11, the bound electron stopping power is set to some low value, since free electron stopping dominates.

From an energetics point of view, errors in the low energy regime are not as critical as at higher energies. For example, a proton with an initial energy of one MeV has lost 90% of its energy and is near the end of its range by the time it degrades to a 0.1 MeV proton. Therefore, errors in stopping power below 0.1 MeV will not affect energy deposition profiles very much.

### (2) Interaction With Free Electrons

For heated target materials, the atoms become ionized, and stopping due to free electrons must be considered. The free electron stopping power is calculated from

$$\left(\frac{dE}{dx}\right)_e = \frac{\rho(x)}{m_I} S_f(V),$$ (21)

with

$$S_f(V) = \frac{2\pi e^4 Z_B^2 \bar{Z}}{mV^2} F(\xi) \left\{ \ln\left(1 + \frac{D^2}{b^2}\right) + \ln\left(1 + 4\xi^2\right) \right\},$$ (22)

where $\bar{Z}$ is the average charge of the target ions, D is the Debye shielding length, and

$$\xi = (m_B V^2/2kT)^{1/2},$$ (23)

11

where kT is the electron temperature, and

$$F(\xi) = erf(\xi) - 2 \xi e^{-\xi^2} / \sqrt{\pi} . \tag{24}$$

The quantity b is the minimum impact parameter for electron-ion scattering and is given by

$$b = MAX \left\{ \frac{Z_B e^2}{mV^2} , \frac{\hbar}{2mV} \right\} , \tag{25}$$

i.e., the maximum of either the classical or quantum-mechanical impact parameter defined by the uncertainty principle.

The first term in $S_f(V)$ is the short range ion-electron binary-encounter scattering term and is taken from the work of Campbell,[26] who adapted it from Brueckner and Brysk.[27] The second term is the polarization term and is taken from Pines and Bohm.[28] For distances larger than D, the plasma acts as a continuous medium, and distant collisions cause loss of energy by the excitation of plasma oscillations, which appear as an oscillating wake behind the projectile.

(3) Interaction with Plasma Ions

For stopping power due to the plasma ions, a expression taken from Campbell[26] and Mehlhorn[18] is used;

$$\left(\frac{dE}{dx}\right)_i = \frac{\rho(x)}{m_i} S_i(V), \tag{26}$$

where

$$S_i(V) = \frac{4\pi e^4 Z_B^2 \bar{Z}^2}{m_I V^2} \ell n \Lambda F(\xi) \tag{27}$$

where

$$\xi^2 = m_I V^2 / 2kT_i , \tag{28}$$

12

$$F(\xi) = erf(\xi) - \frac{2}{\sqrt{\pi}} (1 + \frac{m_I}{m_B}) \xi e^{-\xi^2} \qquad (29)$$

$$\ln \Lambda = (1/2) \ln (1 + b_{max}^2 / b_{min}^2) . \qquad (30)$$

$b_{max}$ is set equal to D, and $b_{min}$ is given by

$$b_{min} = MAX \left\{ \frac{z_B \bar{z} e^2}{\mu m_p V^2} ; \frac{\hbar}{2\mu m_p V} \right\} \qquad (31)$$

where $m_p$ is the proton mass, and

$$\mu = \frac{m_B m_I}{m_B + m_I} . \qquad (32)$$

## (4)  Enhanced Stopping Power From Collective Effects

The stopping power of a dense ion beam can differ from the sum of single particle stopping powers.  One way in which this can occur is through phase mixing of the polarization wakes produced in the ambient medium by the beam particles.  The magnitude of this particular effect is similar to that given by McCorkle and Iafrate[29] for electron beams,

$$S_b = S_o (1 + 2\pi n_B a^3/3) \qquad (33)$$

where $S_b$ is the enhanced stopping power, $S_o$ is the single particle stopping power, $n_B$ is the beam number density and a is the ratio of the beam velocity and local plasma frequency

$$a = V_B/\omega_{pe} . \qquad (34)$$

13

For the case considered below, a 1 MeV proton beam with a flux $n_B v_B = 10^{26}$ $cm^{-2}$ $sec^{-1}$ on a solid density aluminum target, the correction to the stopping power is quite small.


III. RESULTS

Two treatments of the proton beam- Al target interaction have been performed. The first used the LOM to calculate bound electron stopping, whereas the second calculation utilized the MPP stopping cross sections. Figures 1 and 2 indicate that these two sources give different stopping powers, particularly at lower proton energies. Thus, two simulations were done to test the effects of these different cross sections. On the assumption that the MPP data are more accurate, the emphasis will be on the results from this treatment. Some comparisons of results from the two simulations will be given.

The interaction of a monoenergetic 1 MeV proton beam with a planar aluminum slab of 15 μm thickness is treated in this investigation. The beam is assumed to consist of a square-shaped pulse of 10 nanosecond duration with a flux of $10^{26}$ protons/$cm^2$-sec. The beam intensity on target is $1.6x10^{13}$ W/$cm^2$, which is comparable to the intensities available with current devices.

A slab thickness of 15 μm is chosen because this thickness corresponds to the range of 1 MeV protons in cold solid density Al[30]. Hence, the beam is initially totally stopped within the target and deposits most of its energy near the back surface due to the Bragg peak in the stopping cross sections. However, as may be seen from Figs. 1 and 2 and Table 2, the bound electron stopping power decreases as the Al ion charge increases; hence, as the target temperature rises, and the ion charge increases, the beam penetrates completely through the target until the free electron population rises sufficiently to stop the beam entirely within the plasma.

A point to be noted also in this regard is that, for consistency, the average charge obtained from solving the CRE equation is used throughout the calculation. Continuum lowering is not taken into account. This means that, near solid density, the average charge $\bar{Z}$, and hence the electron

14

density, is probably low. The free electron contribution to stopping power is somewhat underestimated at early times in the plasma evolution. However, on a time scale of the order of nanoseconds, the plasma density is two orders of magnitude below solid density $\rho_s$, and the CRE $\bar{Z}$ is valid.

Figures 3 and 4 show density and temperature profiles at different times as the plasma evolves. As may be noted from these figures, the plasma spreads and becomes more uniform in density and temperature as time increases.

Figure 5 compares density and temperature profiles at one nsec from the treatment using MPP data with the treatment using the LOM model. Use of the smaller MPP cross sections results in deeper penetration by the beam. Hence, the backside density is lower, and the temperature higher, than that which results from use of the LOM stopping power. The LOM result shows a sharper density gradient near the rear surface. Away from the backside, the density and temperature results are reversed; the LOM curves are hotter and less dense due to increased energy deposition in that part of the plasma.

Figure 6 compares density and temperature profiles from the two calculations at about 3 nsec. The MPP density curve is much more uniform now, as is the LOM curve, except that a steep density gradient at the rear surface is still maintained. The LOM still yields higher temperature and lower density.

Figure 7 compares density and temperature profiles at 10 nsec from the two calculations. At this late time, the two profiles are similar. By this time, beam stopping is dominated by free electron stopping, and the difference in the bound electron stopping power models has become irrelevant.

Figures 8 through 11 show calculated spectra from the MPP simulation emitted from the front and rear sides of the plasma. In Fig. 8, at 0.5 nsec, the rear side at temperatures near 40 eV is about twice as hot as the front surface due to peaking of the stopping power near the rear surface. This results in a more intense rearside spectrum. As may be seen from Fig. 4, this situation has reversed at later times, and at 4.31 nsec, the front side is emitting a much more intense spectrum than the rear side. The peak intensity on the front side has risen two orders of magnitude and shifted to higher photon energies. The rear side intensity has also increased, but

15

less dramatically. Some K shell emission in the region around one to two keV can be noted.

Front and rearside spectra at about 10 nsec (when the beam is shut off) are shown in Fig. 10. The front side spectrum is very similar to the 4.31 nsec spectrum, but the near side intensity has increased as the plasma continues heating and becomes more uniform [see Figs. 3 and 4]. K shell emission is very prominent here. Figure 11 shows spectra at 18 nsec when the plasma has cooled considerably and has become very uniform. The spectra from both sides are very similar and have been reduced from the 10 nsec levels.

For the sake of comparisons, front and rear spectra at one nsec from the MPP simulation and from the LOM simulation are shown in Figs. 12 and 13. As in Fig. 8 for the MPP simulation at 0.5 nsec, Fig. 12 shows the backside emission to be more intense. As can be noted from Fig. 5, the rear surface is hotter and slightly more dense than the front surface. In Fig. 13, the situation is reversed, with the front surface being the stronger emitter than the rear surface in the LOM case. From Fig. 5, for this situation, the front surface is hotter and much less dense. In Figs. 12 and 13, the front side spectra are very similar due to similar density and temperature, but the rear MPP spectra are much more intense due to higher temperature and lower density.

Figure 14 shows front and rear spectra at about 10 nsec from the LOM simulation. Comparison with Fig. 10 shows these spectra to be very similar to the MPP spectra at the same time. This results agrees with Fig. 7, where it was seen that the 10 nsec density and temperature profiles from the two calculations are very similar. Thus it may be concluded that at late times, the differences in the two atomic electron stopping powers do not contribute substantially to the results, particularly diagnostic tools like spectra.

Figure 15 shows the energy history of the plasma and the partitioning of that energy. At early times, the radiated power is an insignificant fraction of the beam energy, but at late times, it becomes a significant portion of the energy budget. At about 12 nsec, it equals then surpasses the total energy (sum of kinetic, potential, and thermal energies) in the plasma; beyond this point, more of the deposited energy has been radiated away than remains in the plasma.

16

To investigate the importance of radiation transport, the MPP simulation was repeated, but with radiation transport omitted. Fig. 16 shows temperature and density profiles at 3 nsec with and without radiation. Including radiation effects produces a more uniformly-dense plasma in this case. The densities are not very different, except that the profile without radiation shows a dip in the center and a much less dense blow off region in the front. The radiationless temperature profile also attains a higher maximum value.

Figure 17 shows similar comparison at 10 nsec. Both density profiles exhibit gradients near the rear surface, but the radiationless density gradient is much steeper, and has a lower density blow off region in the front. Because there is no energy loss due to radiation, much higher temperatures result.

Figure 18 shows the temperature and density of the rearside of the plasma as a function of time when radiation is included and when it is omitted. The curves are very similar until about 4 nsec; after this time the rear side is denser and cooler when radiation is omitted. Since, at these times, the beam is stopped in the plasma well before it reaches the back side, the large temperature difference between 4 nsec and 10 nsec indicates that radiation transport plays a significant role in heating the rear side. This agrees with a conclusion reached in a study of the interaction of a $10^{13}$ W/cm$^2$ laser pulse at 1.06 μm wavelength on 8.0 μm Al [Duston, et.al[31]].

The density and temperature rise around 9 nsec in the radiationless case is due both to a shock reaching the rear surface and to deeper penetration by the beam. This deeper penetration results from generally lower plasma densities at later times than when radiation is included (e.g., see Fig. 17). Rearside heating at this time is due primarily to convection. In the other treatment, the beam is still being stopped near the center of the plasma, but radiation transport is keeping the rear side at a high temperature even after the beam turns off at 10 nsec.

Fig. 19 shows the time behavior of the density and temperature of the front side of the plasma. Here the effects of radiation transport are more pronounced; the radiationless case produces much higher temperatures and much lower densities. The marked drop in temperature after 10 nsec is due to radiative cooling in the case where it is included.

17

Fig. 20 gives the energy history of the plasma along with the energy partitioning for the radiationless case. The plasma energy is equal to the deposited energy at all times. The thermal energy is much higher than in Fig. 15 for the radiation-hydro case; this indicates that radiation cooling occurs at the expense of the plasma thermal energy. This is also indicated by the much higher temperatures in the radiationless curves in Figs. 16-17. The ionization energies are not very different in the two calculations. The radiationless case has higher kinetic energy at later times; this accounts for the greater widths of the hydrodynamic plasma.

These comparisons of the radiationless and hydro-radiation transport cases clearly establish the importance of radiation transport effects in hot plasmas. <u>Any realistic treatment of hot plasmas must include self-consistent radiation effects.</u>

## IV. <u>COMPARISON WITH LASER-TARGET INTERACTION</u>

It is of interest to make some qualitative comparisons with a simulation of a laser-aluminum target interaction at roughly the same incident energy intensity. Duston, et. al.[31] studied the interaction of a 1.06 micron laser beam at an intensity of $10^{13}$ W/cm$^2$ and a long pulse length (3 nsec full width at half maximum) with an 8 μm thick aluminum foil. Fig. 21 is taken from that study.

In the laser case, after the initial blow off plasma is formed, the beam does not penetrate into the target beyond the critical density surface, whereas the ion beam penetrates deep into the target, at least at early times. In both cases, the dense part of the plasma at later times is heated predominantly by radiation transport rather than thermal conduction. The laser case shows much lower densities and higher temperatures on the front side of the plasma, whereas on the backside the laser case shows much higher density and lower tempertures. Also, by comparing Figs. 3 and 21, it can be seen that the laser beam calculation produces much sharper density and temperature gradients. These results substantiate the view that proton beams are more efficient than laser beams for heating up the interior and backside of targets; this is due to deeper penetration into the target by the ion beams.

## V. SUMMARY

A fully self-consistent, one-dimensional treatment of the interaction of a one-MeV proton beam with an aluminum slab has been presented. A fully self-consistent hydrodynamic-ionization-radiation transport model was used. The atomic populations as functions of density and temperature were obtained from a collisional-radiative-equilibrium assumption. Radiation transport was calculated using a hybrid scheme that combines a multi-frequency formalism for the continuum with a probability-of-escape method for the lines.

Profiles of the plasma density and temperature at various times in the plasma evolution have been presented. Calculated spectral emissions from the front and rear surfaces at varius times have also been presented.

A simulation involving bound electron stopping power derived from a local-oscillator-model (LOM) has been compared with a simulation involving the detailed stopping cross sections of McGuire, Peek, and Pitchford (MPP), which are generally lower at lower proton energies. At early times (of the order of a nanosecond), the different stopping powers produce different profiles and spectra (see Figs. 5-6 and Fig.s 12-13), but at later times, free electron stopping dominates bound electron stopping (for this particular combination of beam power and slab thickness and the differences in the two simulations disappear (see Figs. 7, 10, and 14).

Comparisons with calculations omitting radiation show that radiation transport can significantly affect plasma evolution, leading to substantially different temperature and density profiles, and must be included in any self-consistent treatment of ion beam-target interactions.

Qualitative comparisons of the ion beam-slab interaction with a treatment[31] of a laser beam-slab interaction shows that the laser produces higher temperatures and lower densities on the front (beam) side of the plasma, while the proton beam is more efficient at heating up the back side due to deeper penetration into the target.

Since these treatments of the beam-target interaction are one-dimensional, energy flow normal to the direction of the beam has been neglected; in addition, self-field effects have not been considered. These effects could alter the range significantly, and alter the magnitude and

shapes of the plasma profiles given here. A two-dimensional radiation hydrodynamics code will be used to investigate some of these effects in a separate paper.

## ACKNOWLEDGMENTS

Table 1 — Least-square-fitting parameters to the MPP stopping powers*

| $q$ | $A_q$ | | $B_q$ | | $C_q$ | | $D_q$ | |
|---|---|---|---|---|---|---|---|---|
| 0 | 3.135 | | −4.415 | (−1) | −2.592 | (−2) | −1.031 | (−3) |
| 1 | 2.773 | | −3.534 | (−1) | −3.719 | (−2) | −5.234 | (−4) |
| 2 | 2.159 | | −8.853 | (−2) | −9.409 | (−2) | 3.625 | (−3) |
| 3 | 1.012 | | 6.257 | (−1) | −2.644 | (−1) | 1.651 | (−2) |
| 4 | 8.459 | (−1) | 5.977 | (−1) | −2.480 | (−1) | 1.482 | (−2) |
| 5 | 6.575 | (−1) | 5.506 | (−1) | −2.331 | (−1) | 1.374 | (−2) |
| 6 | 5.423 | (−1) | 4.501 | (−1) | −2.085 | (−1) | 1.212 | (−2) |
| 7 | 4.447 | (−1) | 2.828 | (−1) | −1.564 | (−1) | 7.782 | (−3) |
| 8 | 3.716 | (−1) | 8.571 | (−2) | −1.072 | (−1) | 4.287 | (−3) |
| 9 | 3.148 | (−1) | −1.870 | (−1) | −3.894 | (−2) | −4.858 | (−4) |
| 10 | −4.684 | (−1) | −2.246 | (−1) | 6.746 | (−3) | −5.082 | (−3) |
| 11 | −7.250 | | 2.867 | | −5.093 | (−1) | 2.388 | (−2) |

* Numbers in parentheses indicates powers of ten

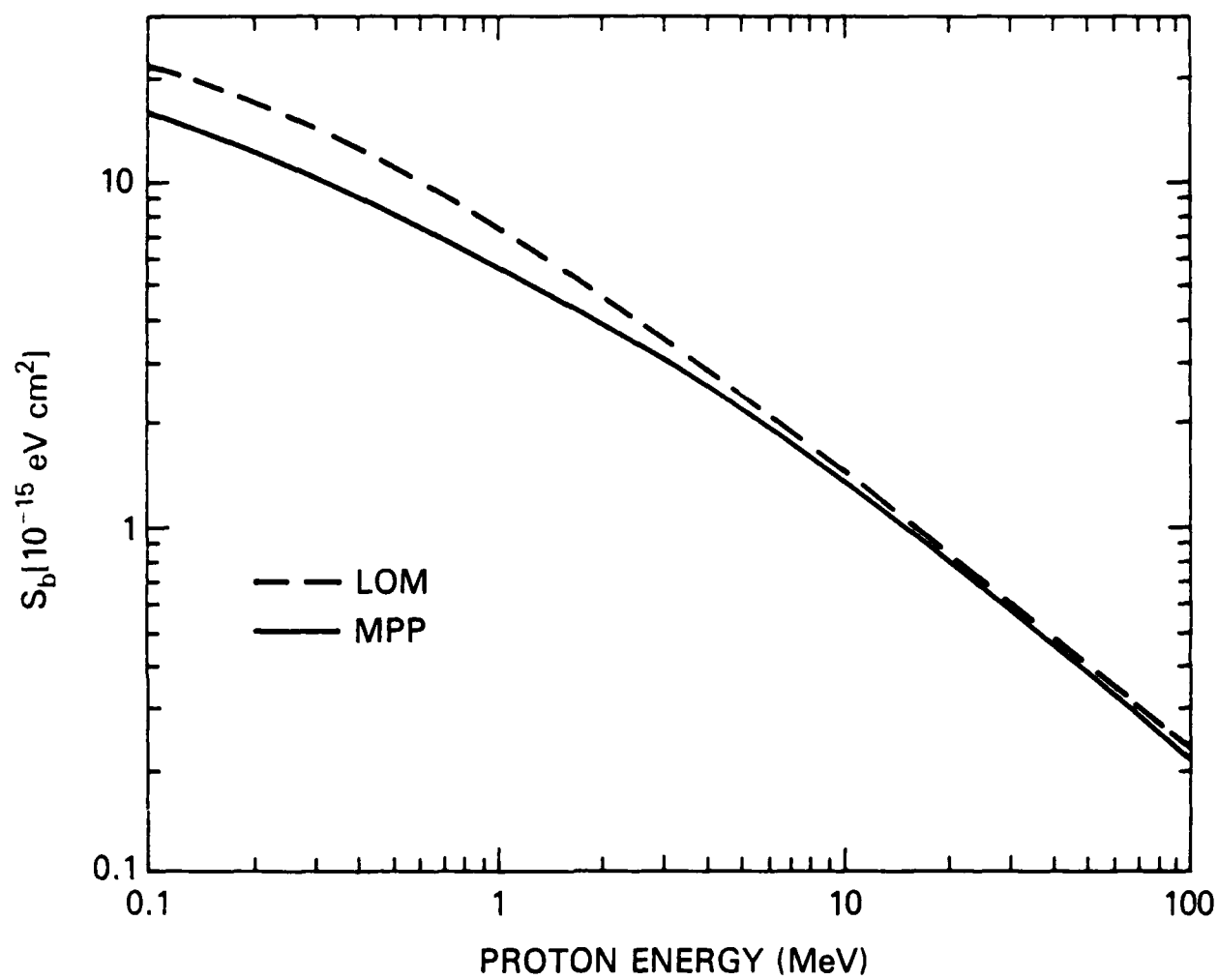Table 2 — Comparison of MPP cross section data with fit results (in units of eV cm$^2$/atom)

Fig. 1  Comparison of MPP and local-oscillator-model stopping cross sections for singly ionized Al.
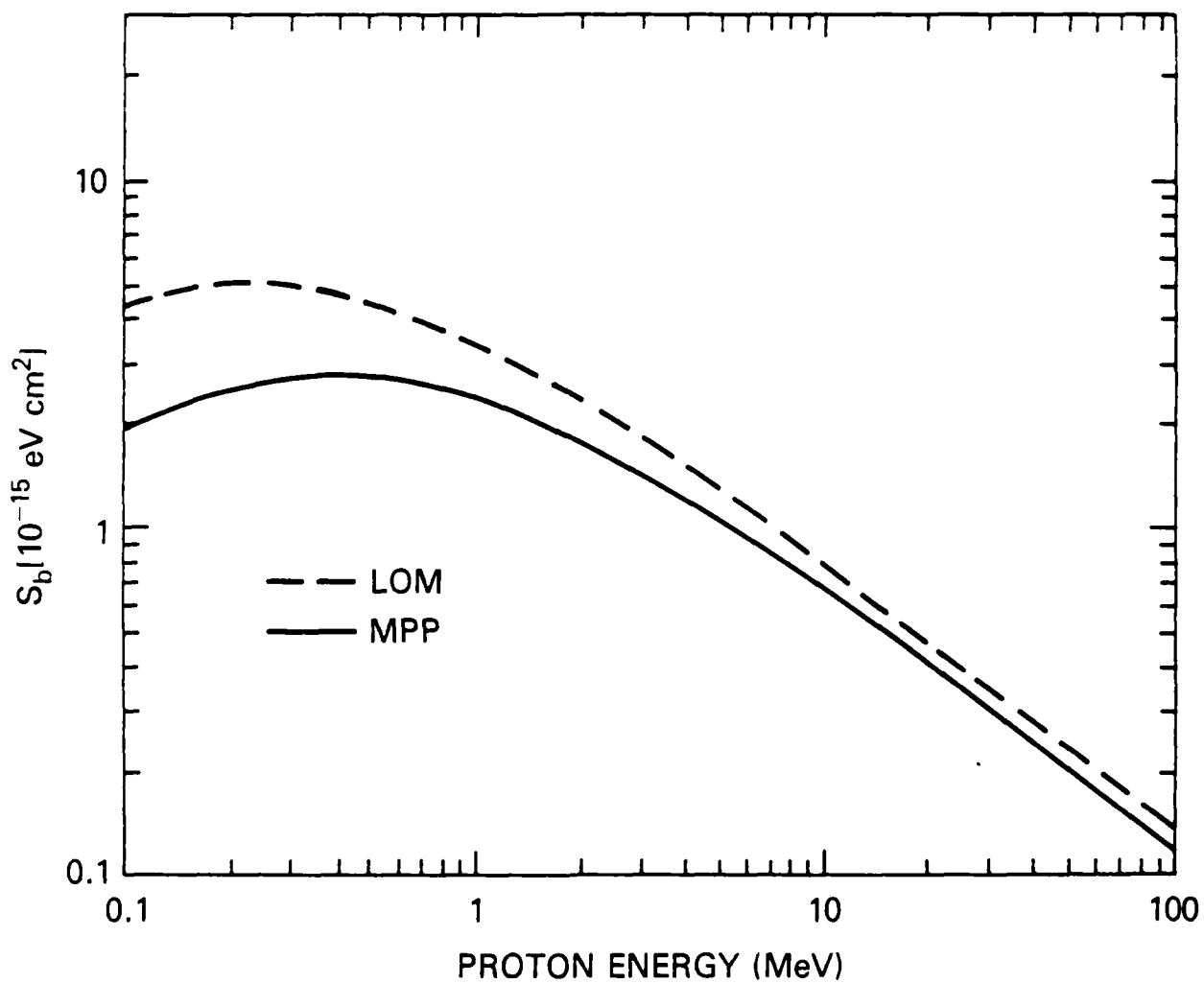
22

Fig. 2. Comparison of MPP and local-oscillator-model stopping cross sections for 5-times-ionized Al.
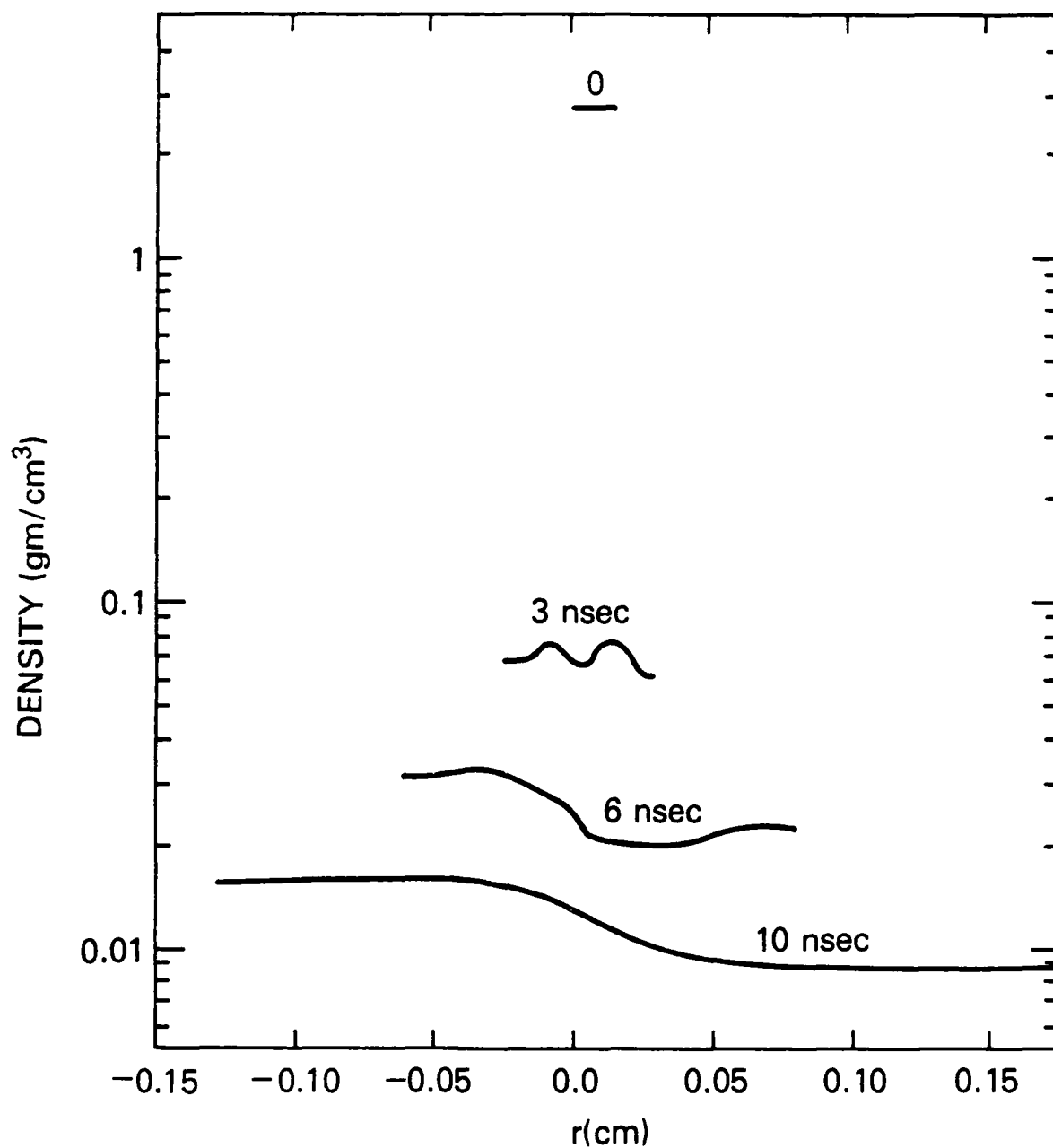
Fig. 3. Density profiles at different times in the plasma evolution using the MPP cross sections.
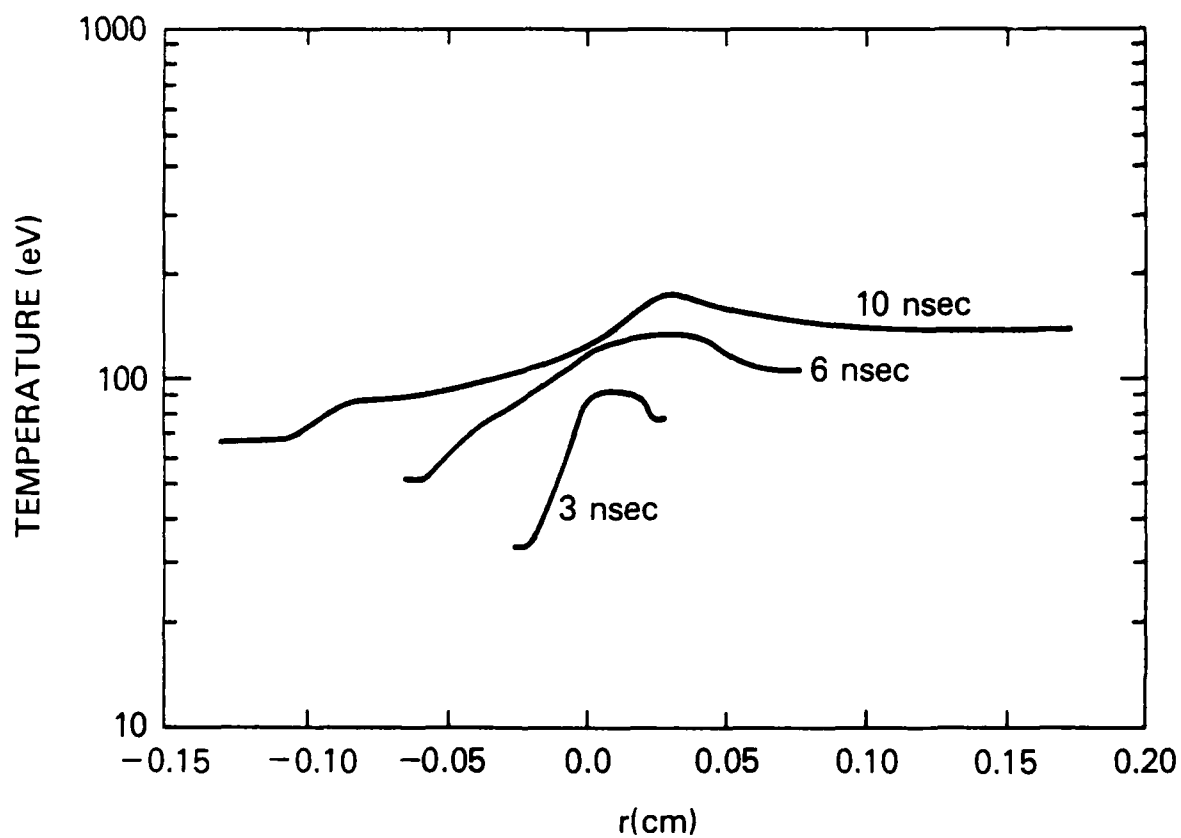
Fig. 4. Temperature profiles at different times in the plasma evolution using the MPP cross sections.
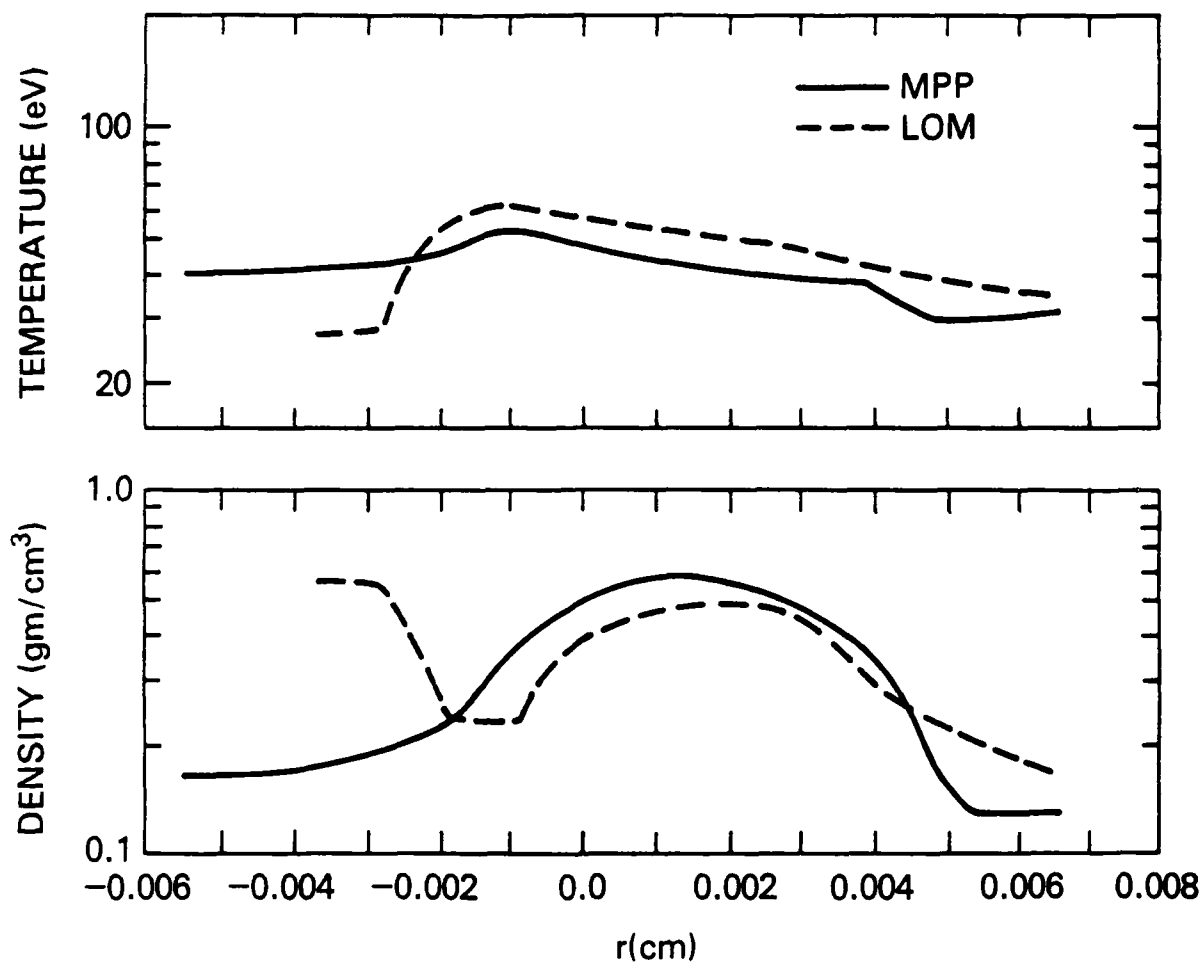
Fig. 5. Comparison of the density and temperature profiles at one nsec from the two simulations using the MPP and LOM cross sections.
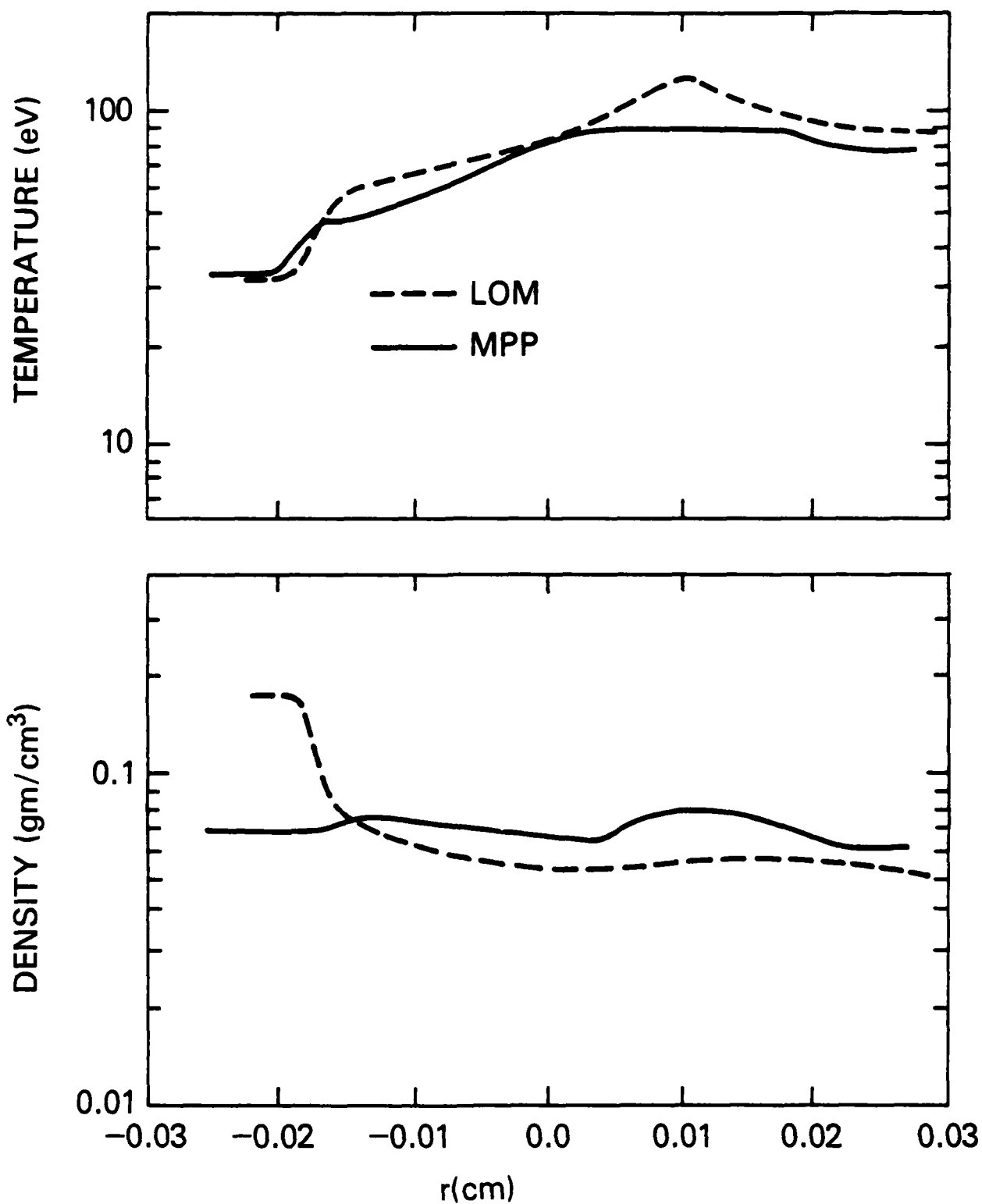
Fig. 6. Comparison of the density and temperature profile for 3 nsec from the two simulations using the MPP and LOM cross sections.
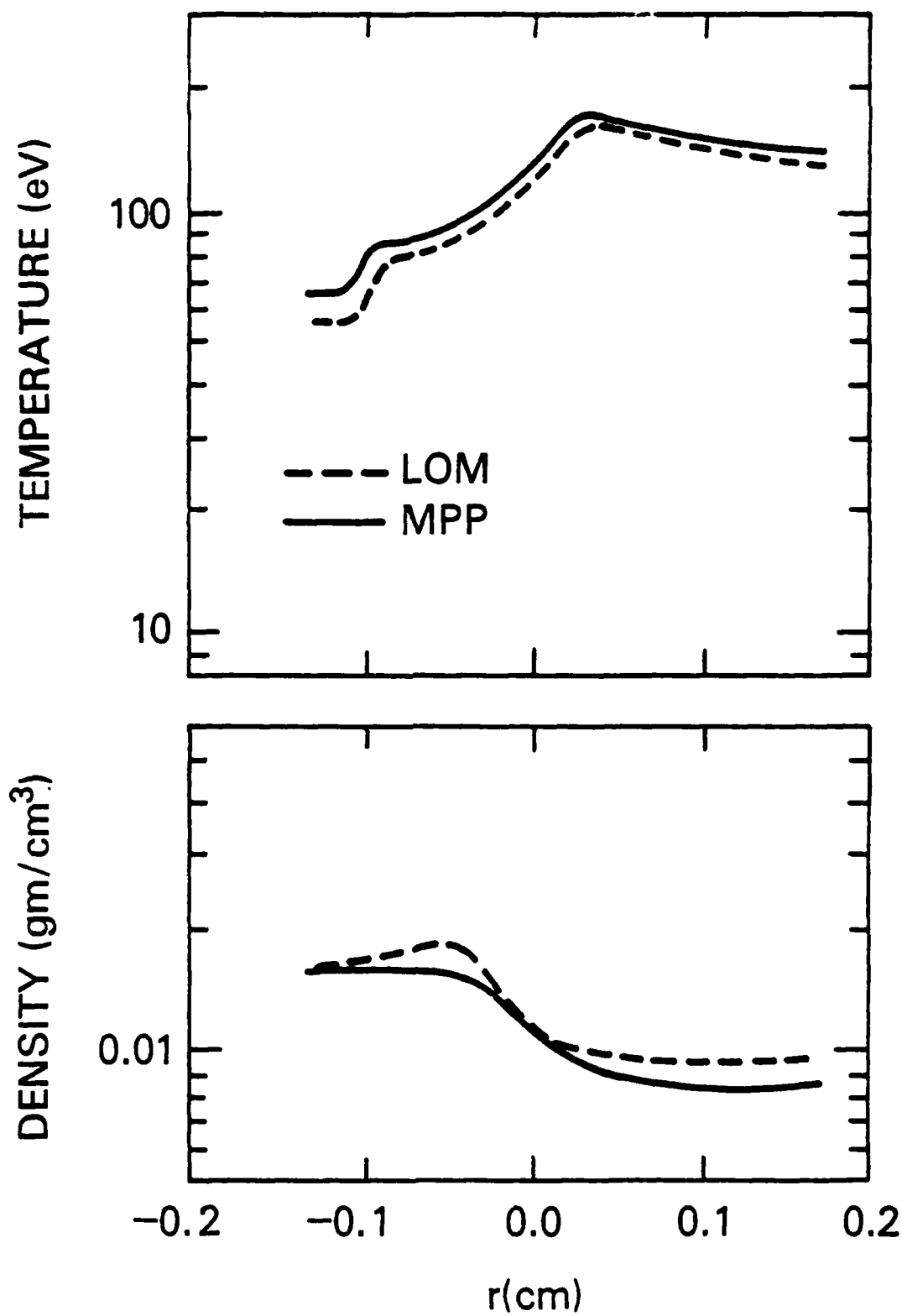
Fig. 7. Comparison of density and temperature profiles for 10 nsec from the two simulations using the MPP and LOM cross sections.
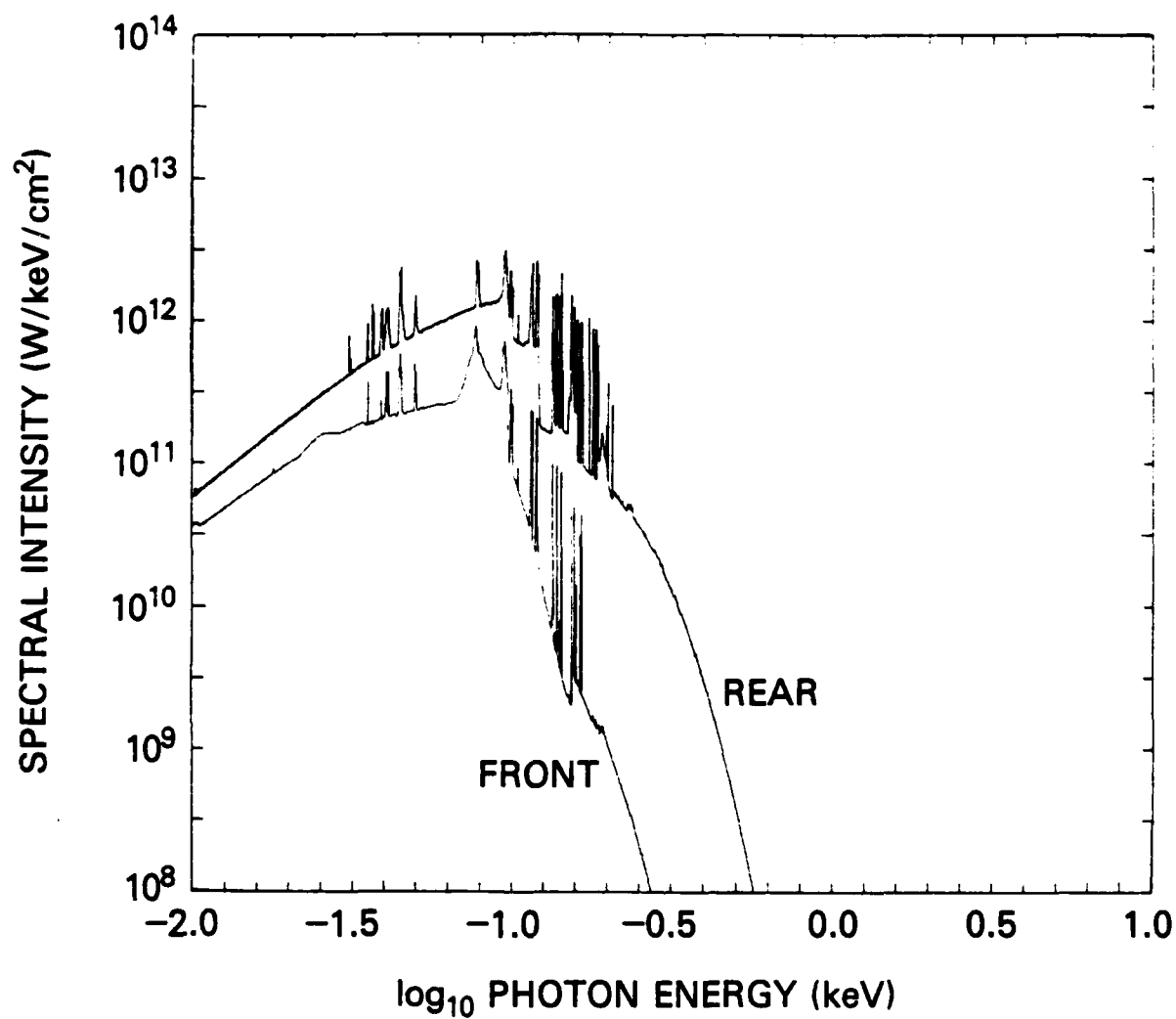
Fig. 8. Front and rear side spectra at 0.5 nsec (MPP cross sections).
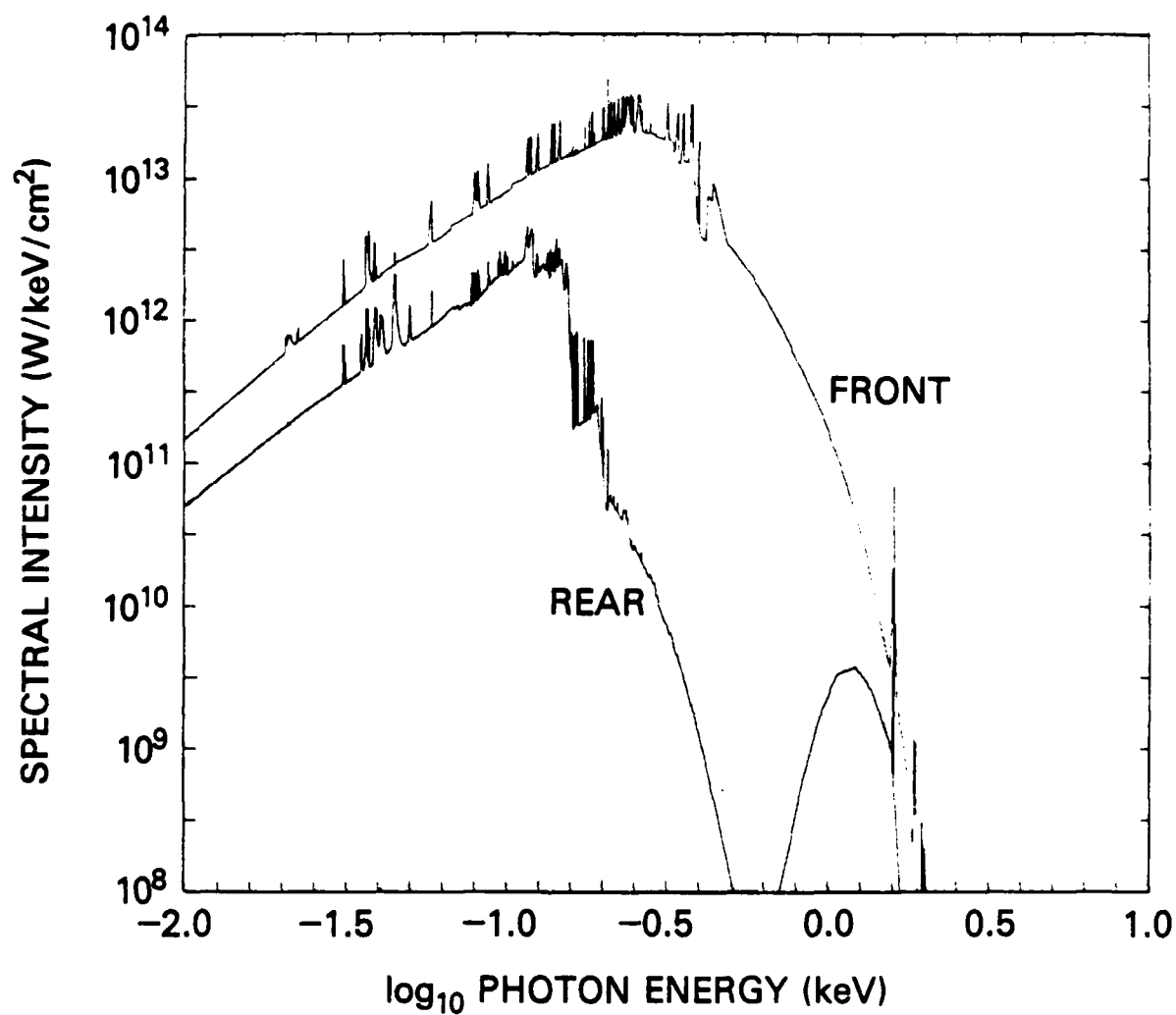
Fig. 9. Front and rear side spectra at 4.31 nsec (MPP cross sections).
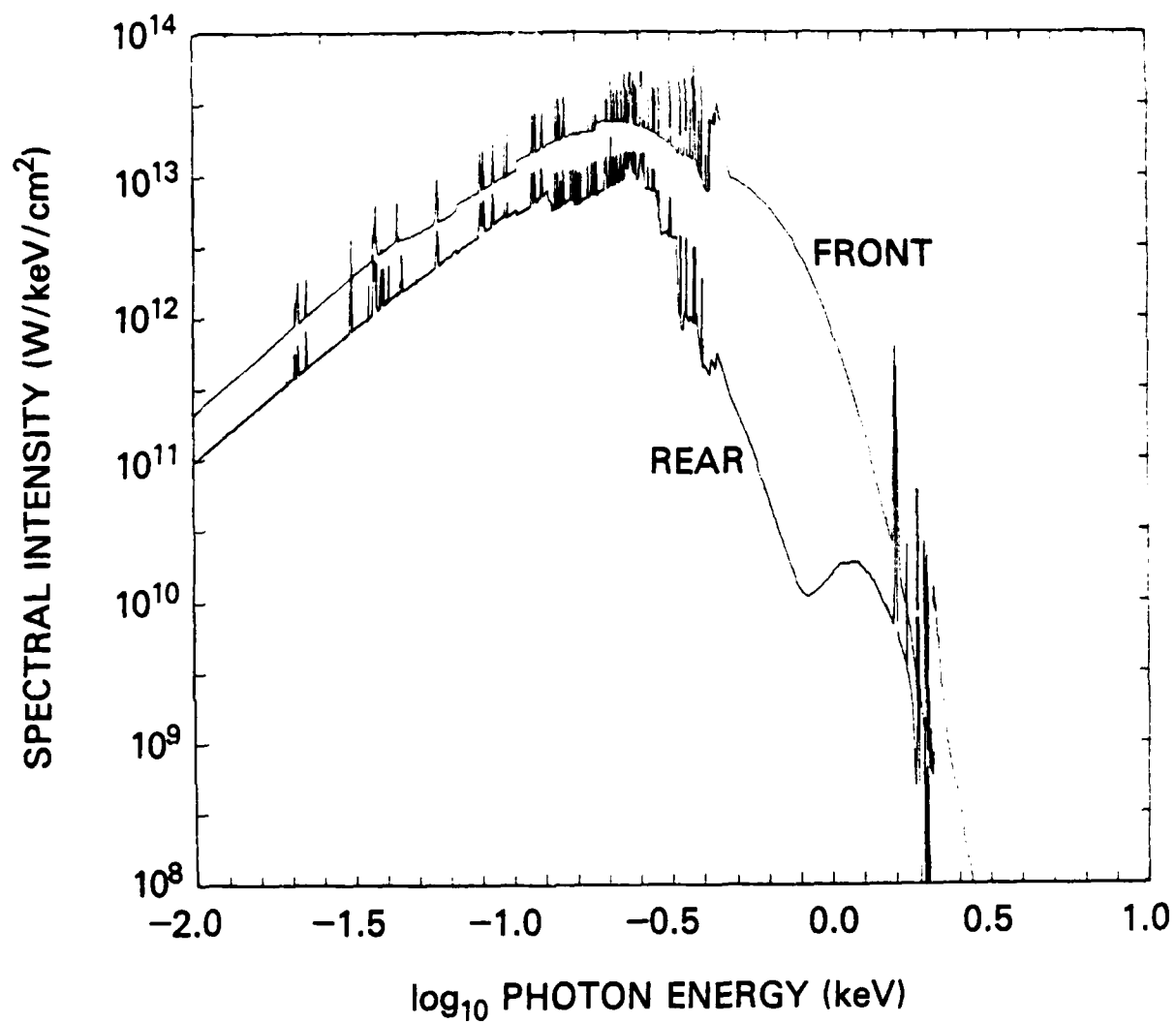
Fig. 10. Front and rear side spectra at 10 nsec (MPP cross sections).

31
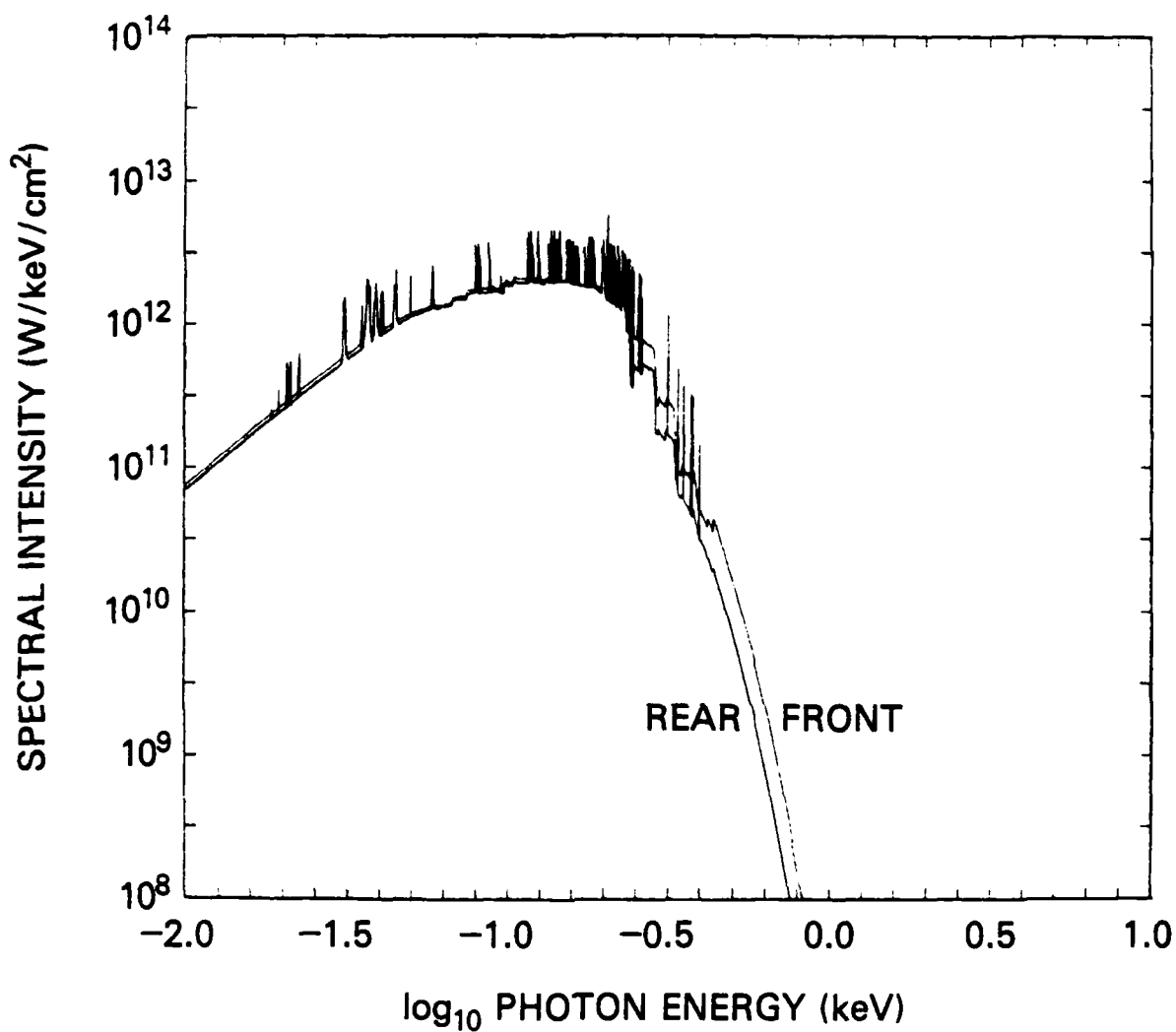
Fig. 11.  Front and rear side spectra at 18 nsec (MPP cross sections).
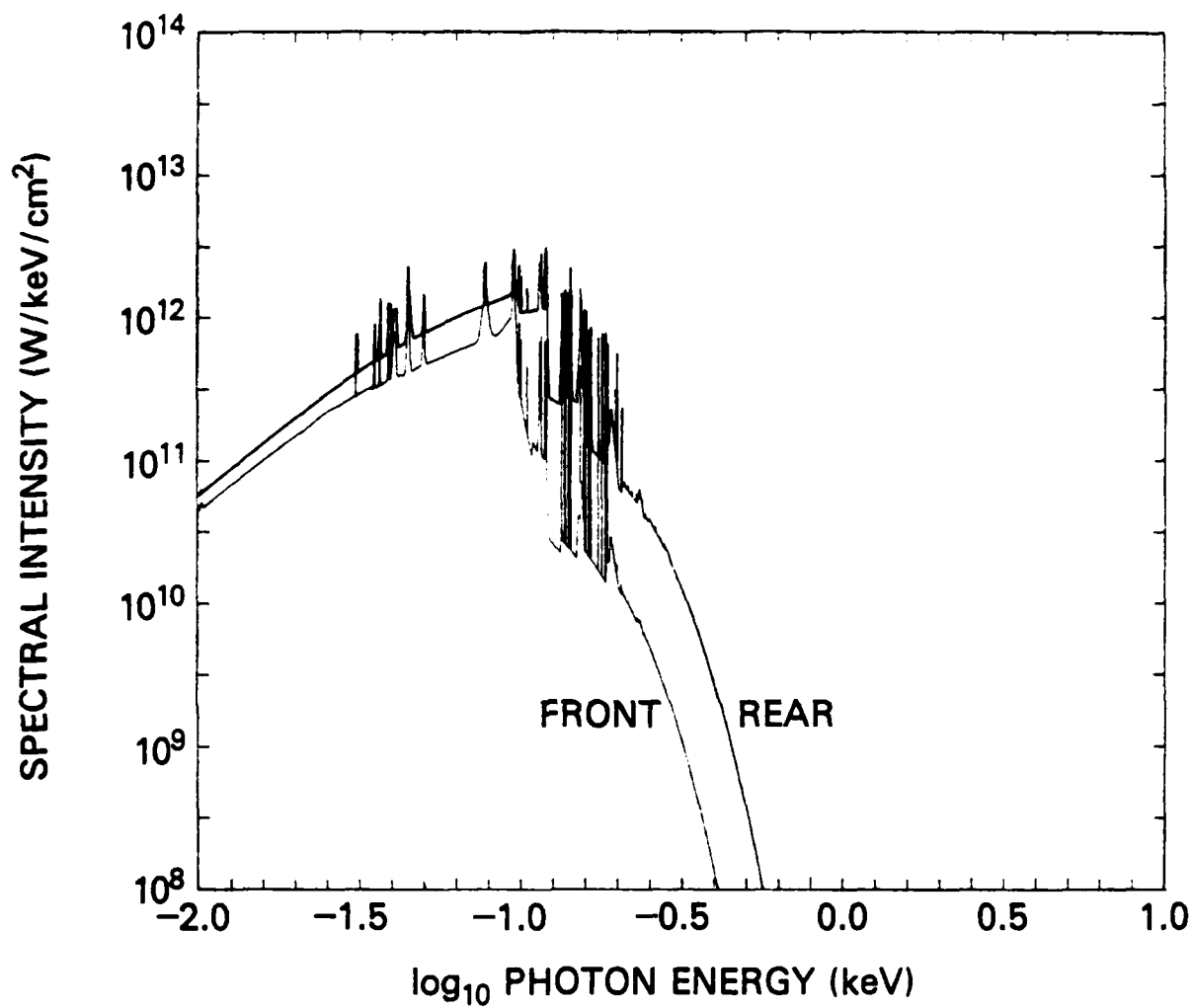
Fig. 12. Front and rear spectra at 1.0 nsec (MPP cross sections).
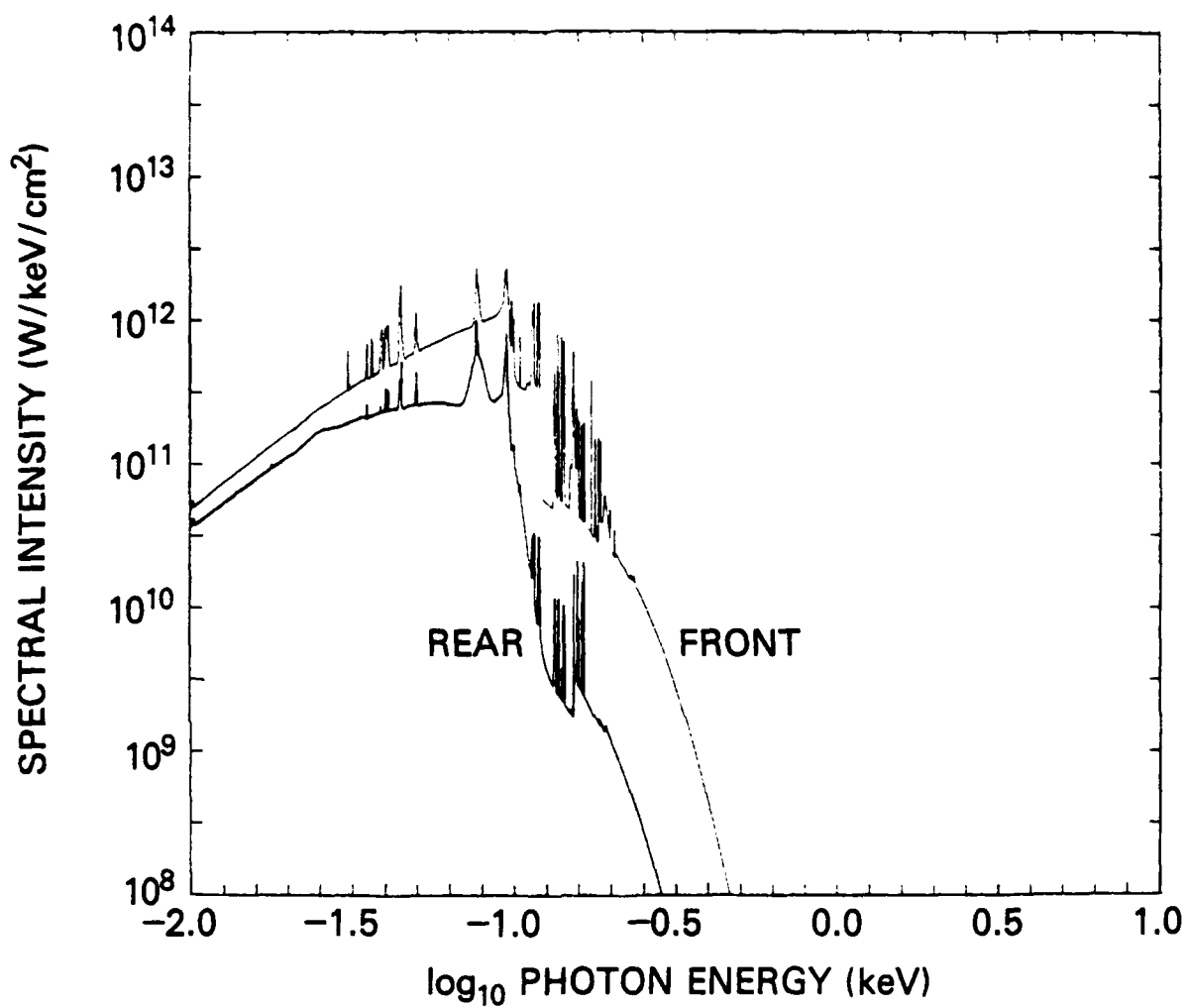
Fig. 13. Front and rear spectra at 1.0 nsec (LOM cross sections).
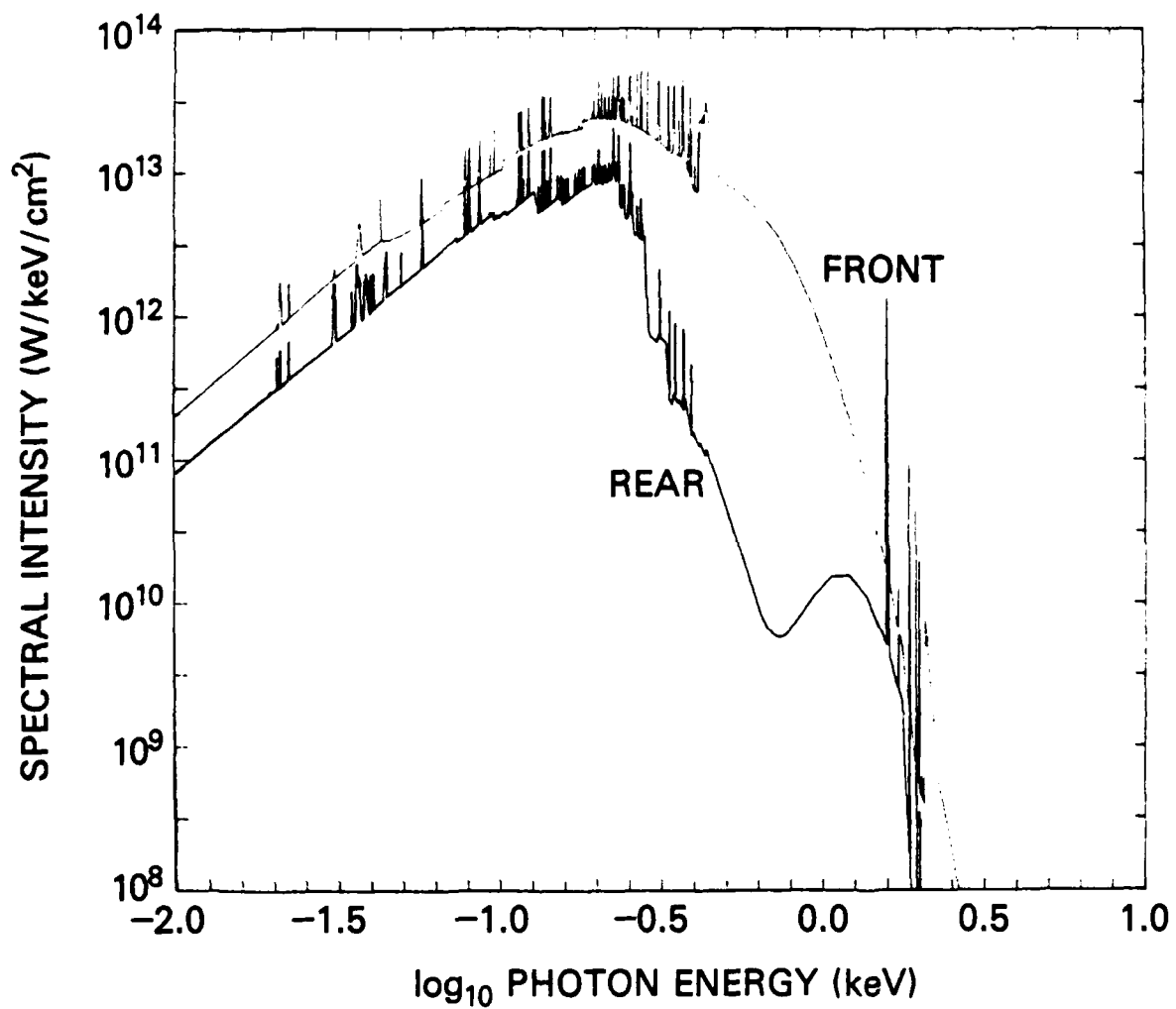
Fig. 14. Front and rear spectra at 10 nsec (LOM cross sections).

35
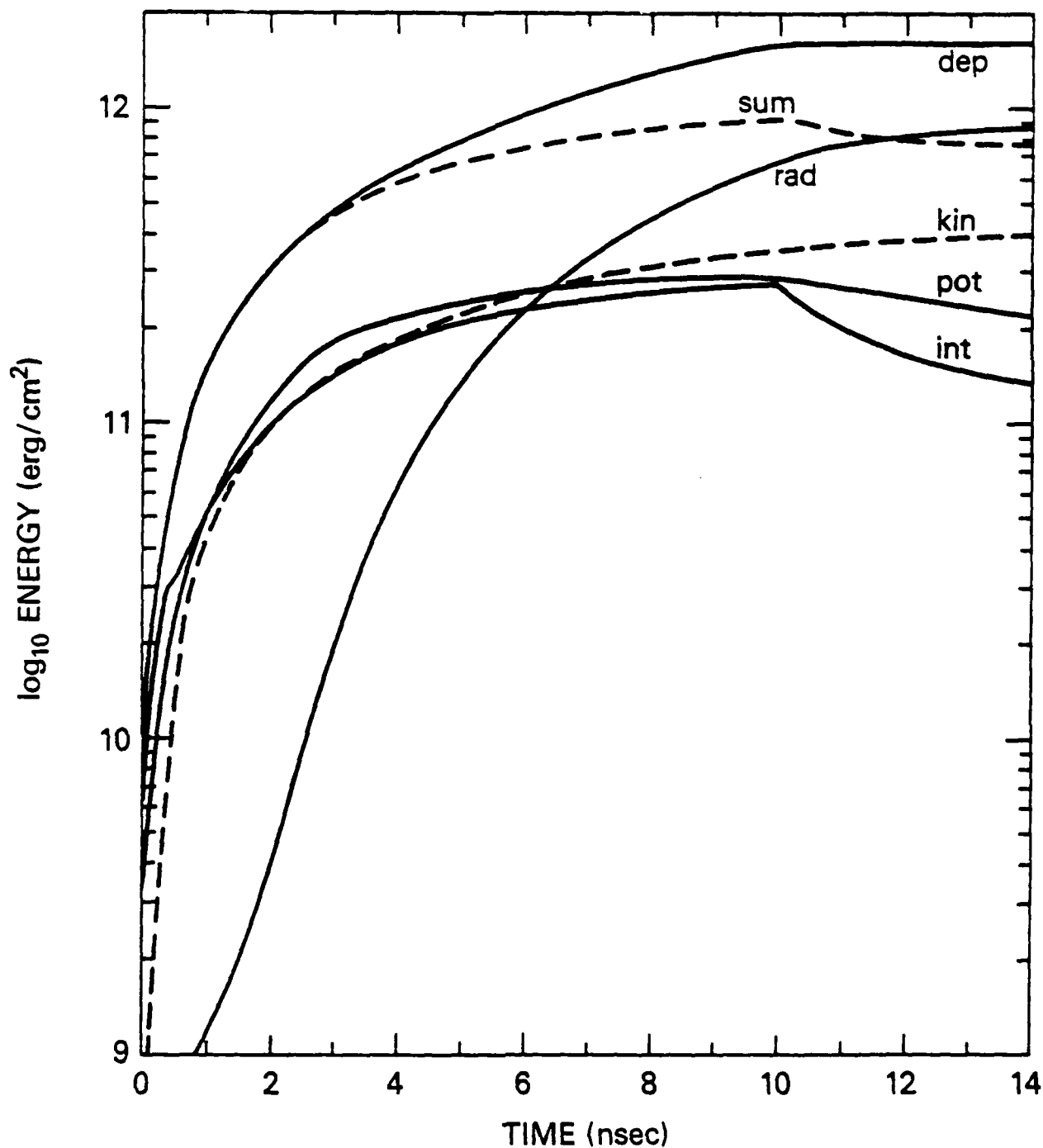
Fig. 15. Energy history of the beam plasma interaction. "dep" is the energy deposited by the beam, and "sum" is the sum of the kinetic, potential, and internal energies. (MPP cross sections).
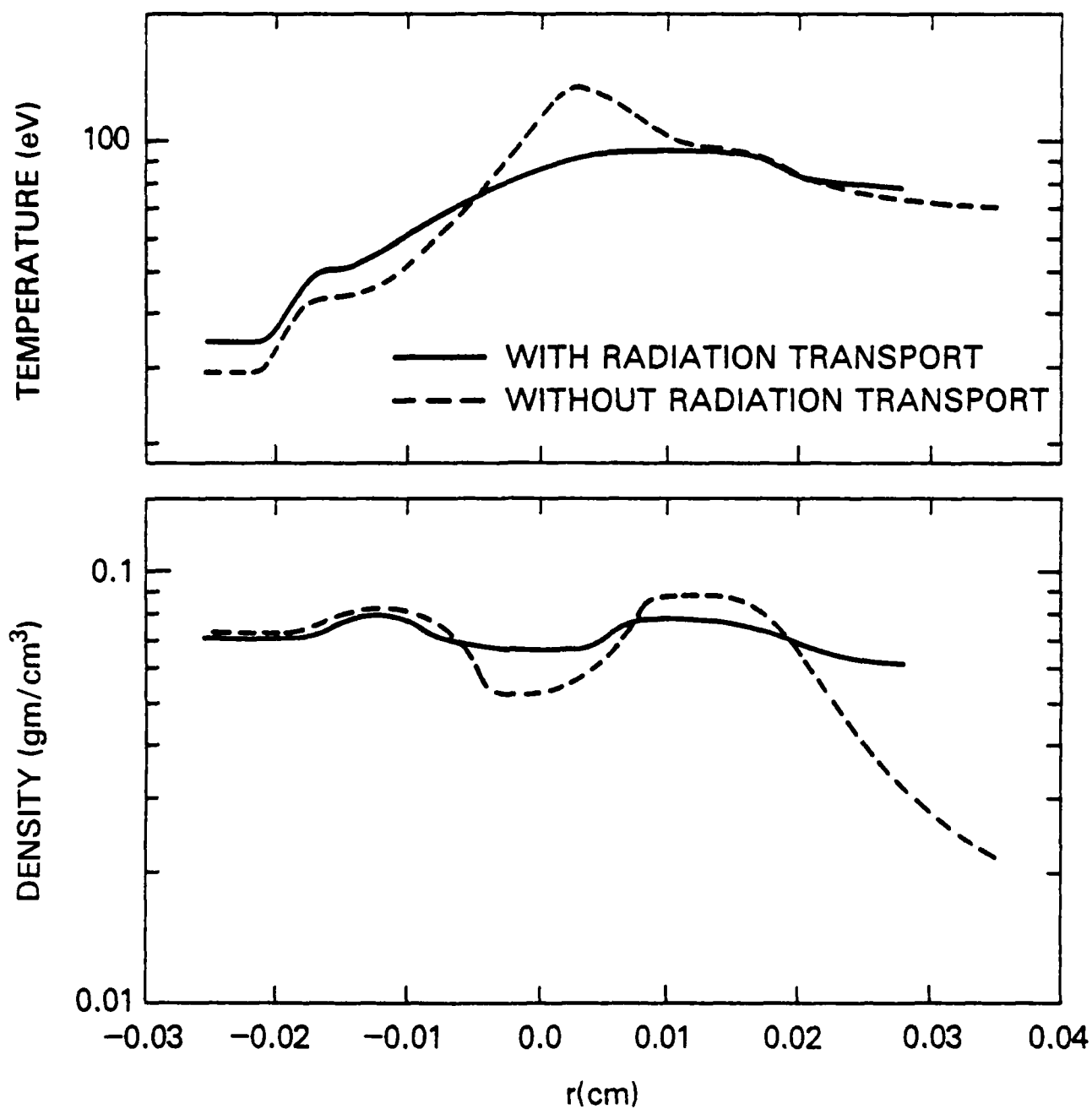
Fig. 16. Comparison of temperature and density profiles at 3 nsec including radiation transport with temperature and density profiles omitting this effect. (MPP cross sections).

37
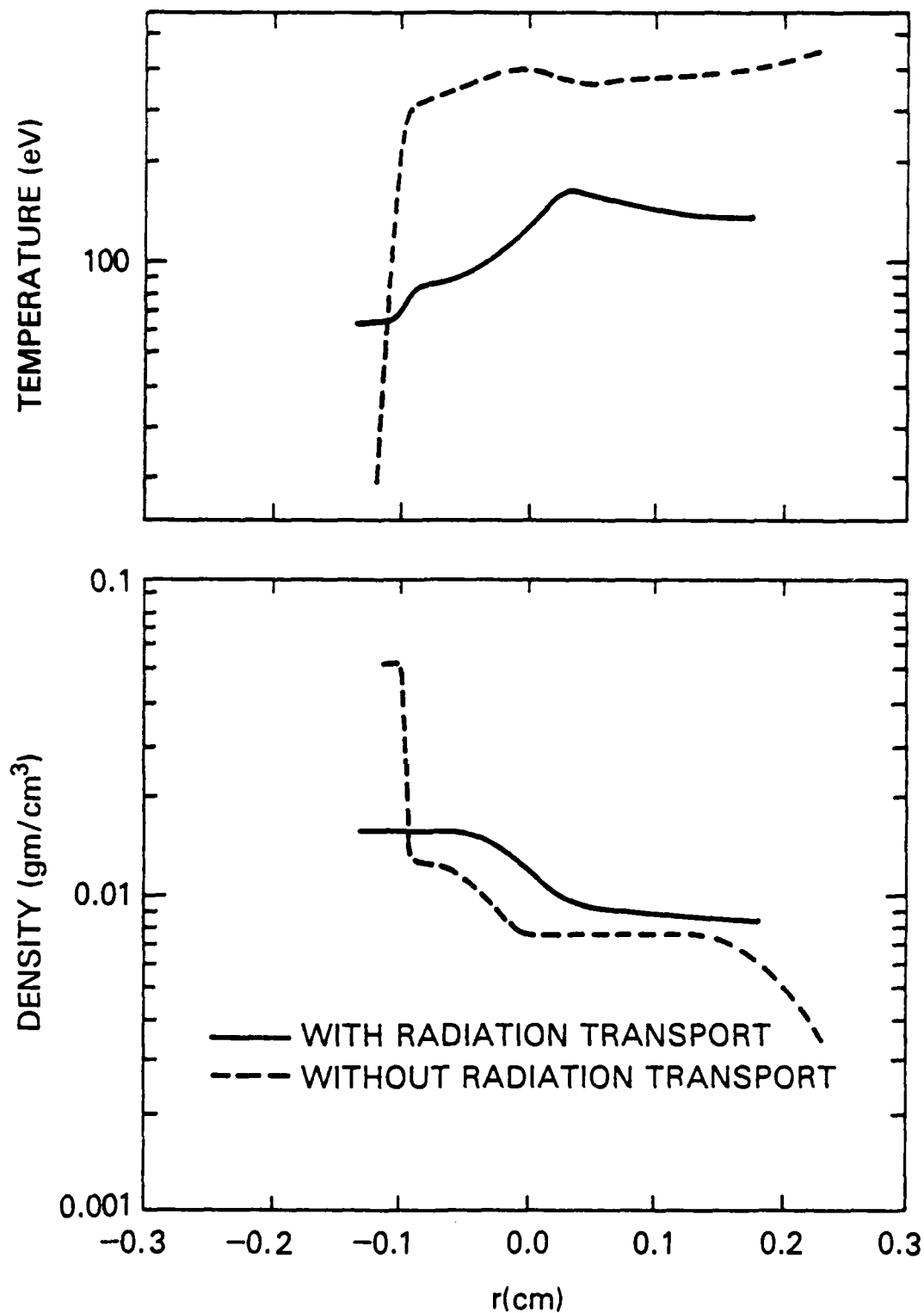
Fig. 17. Comparison of temperature and density profiles at 10 nsec including radiation transport with temperature and density profiles omitting this effect. (MPP cross sections).

38
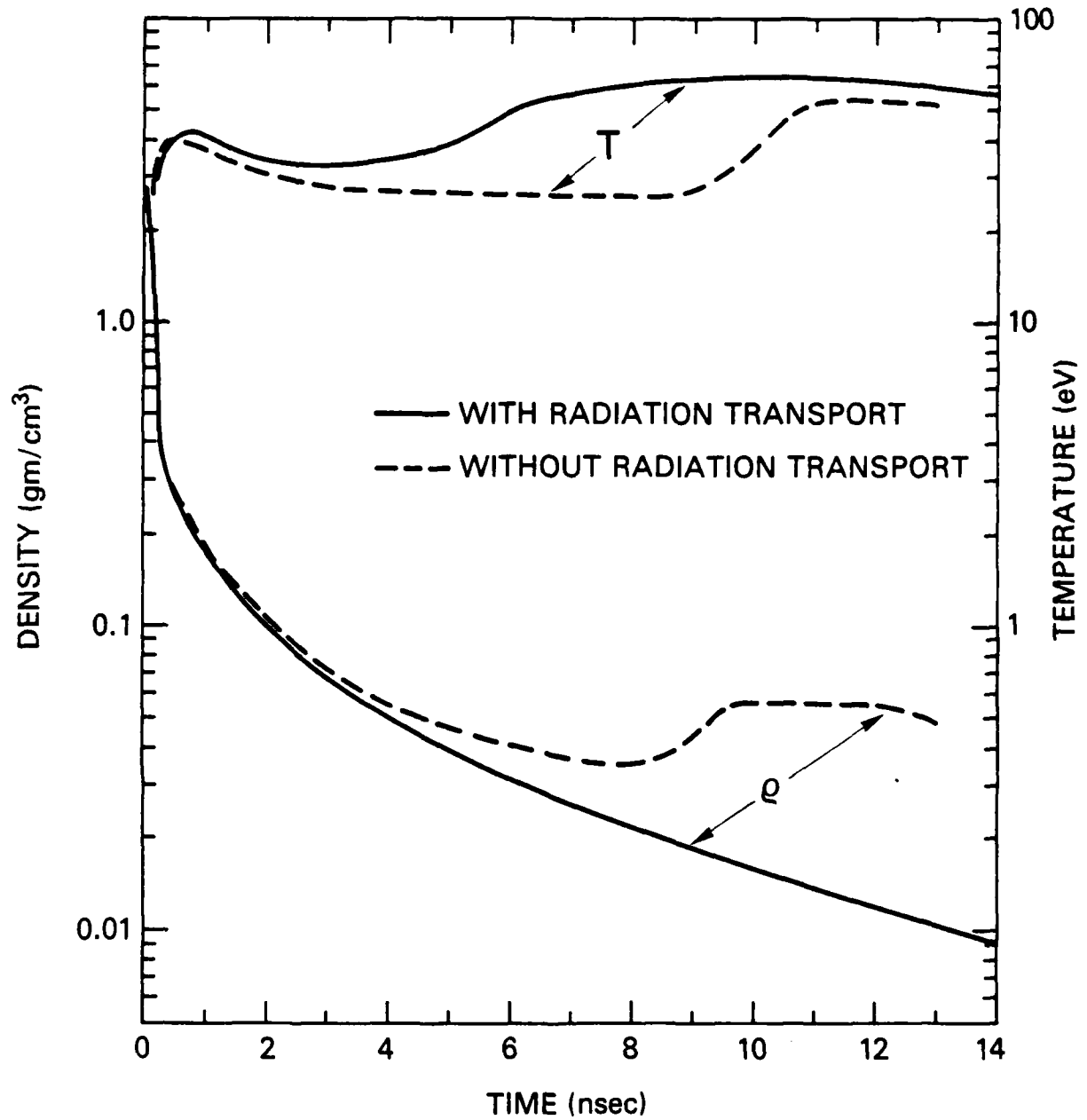
Fig. 18. Temperature and density history of the rear surface of the plasma with and without radiation transport. (MPP cross sections).
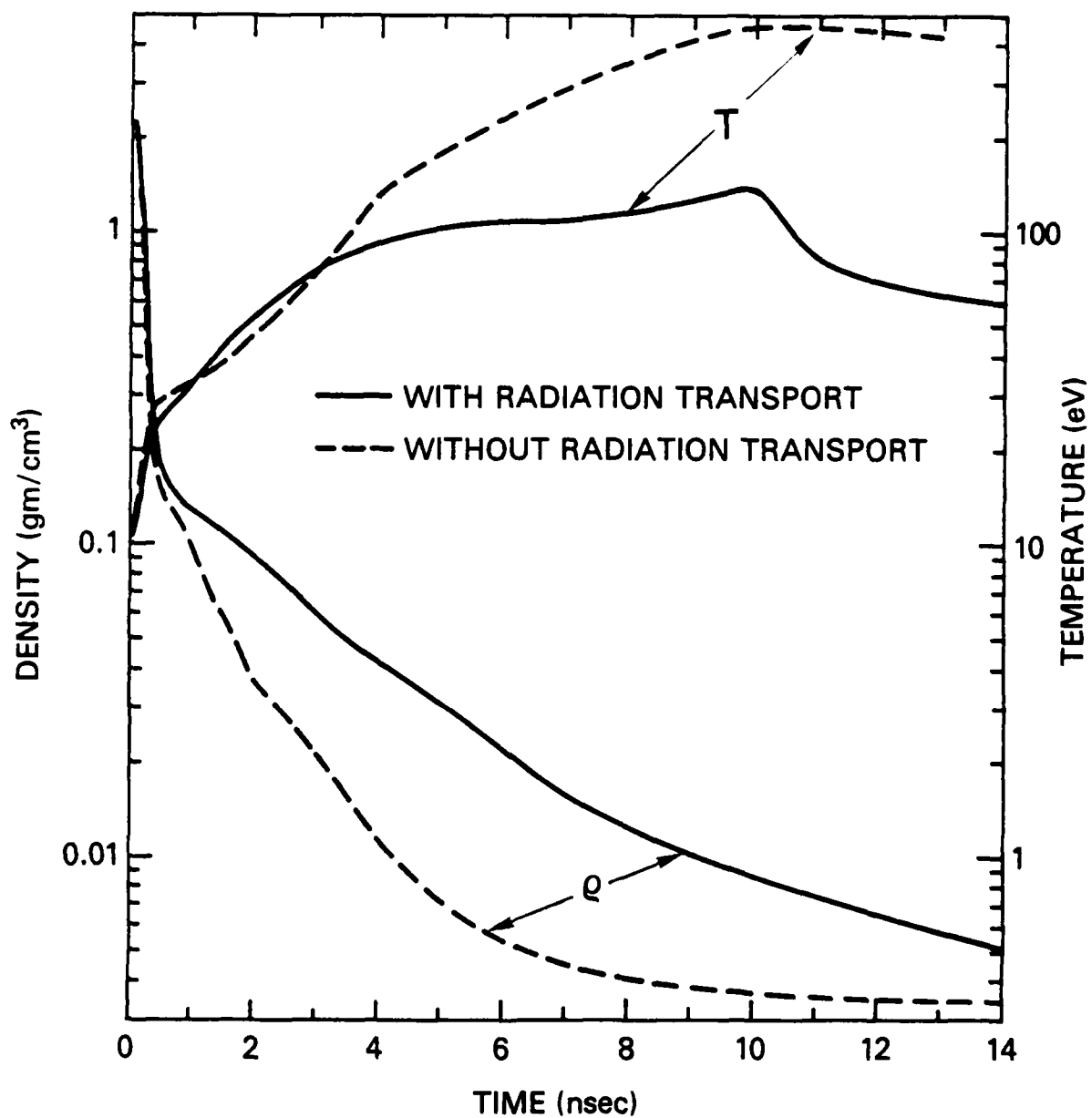
Fig. 19. Temperature and density history of the front surface of the plasma with and without radiation transport. (MPP cross sections).

40
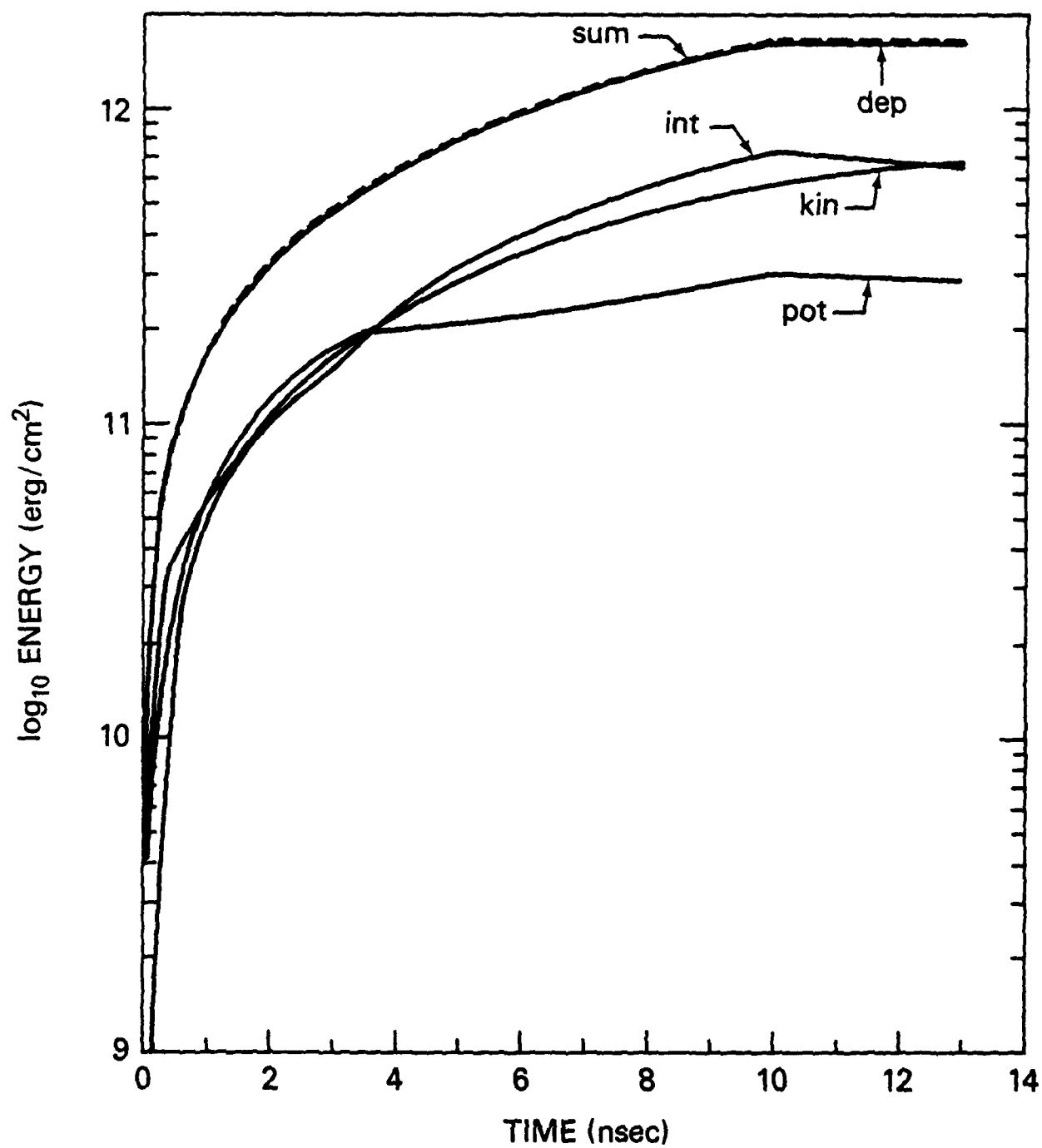
Fig. 20. Energy history of the beam when radiation transport is omitted (same labels as Fig. 15).
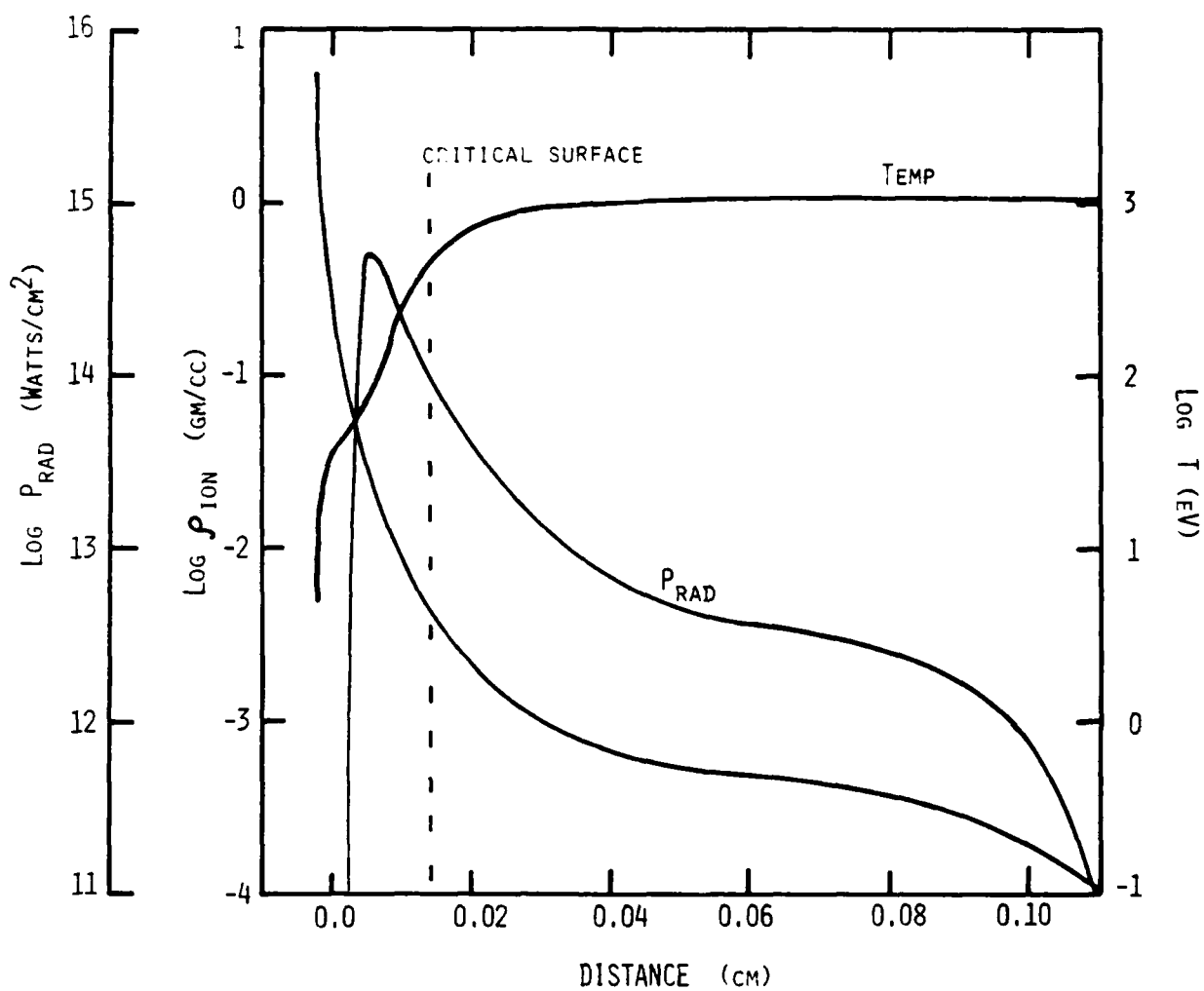
Fig. 21. Temperature, density, and radiative cooling profiles at about 5 nsec in the laser heated foil study [Ref. 31].

# References

1. S. A. Goldstein, G. Cooperstein, R. Lee, D. Mosher, and S. J. Stephanakis, Phys. Rev. Lett. 40, 1504 (1978).

2. H. J. Doucet and J. M. Buzz, eds., High Power Beams 81, Ecole Polytechnique, Palaiseau, France (1981).

3. D. J. Johnson, G. W. Kuswa, A. V. Farnsworth Jr., J. P. Quintez, R. J. Leeper, E. J. T. Burns, and S. Humphries Jr., Phys. Rev. Lett. 42, 610 (1979).

4. J. P. Boris and D. L. Book, J. Comp. Phys. 11, 38 (1973).

5. D. R. Bates, A. E. Kingston and R. W. P. McWhirter, Proc. R. Soc. Lond. A267, 297 (1962).

6. A. Burgess. H. P. Summers, D. M. Cochrane and R. W. P. McWhirter, Mon. Not. R. Astron. Soc. 179, 275 (1977).

7. V. L. Jacobs, J. Davis, P. C. Kepple and M. Blaha, ASTROPHYS, J. 211, 605 (1977).

8. W. J. Karzas and R. Latter, ASTROPHYS. J. Suppl. Ser. 6, No. 55, 167 (1961).

9. V. L. Jacobs and J. Davis, Phys. Rev. A 18, 697 (1978).

10. J. Davis, P. C. Kepple, and M. Blaha, J. Quant. Spectrosc. Rad. Transfer 16, 1043 (1977).

11. E. Oran and J. Davis, J. Appl. Phys. 45, 2480 (1974).

12. D. Duston, and J. Davis, Phys. Rev. A23, 2602 (1981).

13. J. P. Apruzese, J. Davis, D. Duston, and R. W. Clark, Phys. Rev. A 29, 246 (1984).

14. J. P. Apruzese, J. Davis, D. Duston, and K. G. Whitney, J. Quant. Spectrosc. Rad. Transfer 23, 479 (1980); J. P. Apruzese, J. Quant. Spectrosc. Rad. Transfer 25, 419 (1981).

15. J. P. Apruzese, P. C. Kepple, K. G. Whitney, J. Davis, and D. Duston, Phys. Rev. A 24, 1001 (1981).

16. F. Biggs and R. Lighthill, Sandia Laboratories Report No. SC-RR-710507 (1971).

17. E. Clementi and C. Roetti, At. Data and Nucl. Data Tables 14, 177 (1974).

18. T. A. Mehlhorn, J. Appl. Phys. 52, 6522 (1981); Sandia Laboratories Report No. Sand 80-0038 (1980).

19. D. Mosher, in ERDA Summer Study of Heavy Ions for Inertial Fusion, LBL-5543 (1976), p. 39.

20. J. E. Rogerson, NRL Memo Report 4485 (1981). ADA097772

21. R. K. Nesbet and J. F. Ziegler, Appl. Phys. Lett. 31, 810 (1977).

22. J. W. Zink, Phys. Rev. 176, 279 (1968).

23. J. D. Jackson, Classical Electrodynamis, John Wiley and Sons Inc. (1962) p. 643.

24. J. M. Peek, Phys. Rev. A 26, 1030 (1982).

25. E. J. McGuire, J. M. Peek, and L. C. Pitchford, Phys. Rev. A 26, 1318 (1982).

26. P. M. Campbell, "Fast Ion Energy Loss in Dense Plasmas," (1980) (Private communication).

27. K. A. Brueckner and H. Brysk, KMSF Document KMSF - U7 (1971).

28. D. Pines and D. Bohm, Phys. Rev. 85, 338 (1952).

29. R. A. McCorkle and G. J. Iafrate, Phys. Rev. Lett. 39, 1263 (1977).

30. L. C. Northcliffe and R. F. Schilling, Nuclear Data Tables A7, 233 (1970).

31. D. Duston, R. W. Clark, J. Davis and J. P. Apruzese, Phys. Rev. A27, 1441 (1982).

DISTRIBUTION LIST

| | |
|---|---|
| Assistant to the Secretary of Defense<br>Atomic Energy<br>Washington, D.C. 20301<br>    ATTN: Executive Assistant | 1 Copy |

Defense Technical Information Center           2 copies
Cameron Station
5010 Duke Street
Alexandria, Va 22314

Director                                              1 Copy
Defense Intelligence Agency
Washington, D.C. 20301
    ATTN: DT-1B R. Rubenstein

Director
Defense Nuclear Agency
Washington, D.C. 20305
    ATTN: DDST                                  1 copy
    ATTN: TITL                                   4 copies
    ATTN: RAEV                                  1 copy
    ATTN: STVI                                   1 copy

Commander                                     1 Copy
Field Command
Defense Nuclear Agency
Kirtland AFB, New Mexico 87115
    ATTN: FCPR

Chief                                         1 Copy
Field Command
Livermore Division
Department of Defense
P.O. Box 808
Livermore, CA 94550
    ATTN: FCPRL

Director                                         1 Copy
Joint Strat TGT Planning Staff
Offutt AFB
Omaha, Nebraska 68113
    ATTN: JSAS

Undersecretary of Defense                                    1 Copy
  for RSCH and ENGRG
Department of Defense
Washington, D.C.  20301
    ATTN:  Strategic and Space Systems (OS)


Deputy Chief of Staff for RSCH DEV and ACQ                   1 Copy
Department of the Army
Washington, D.C.  20301
    ATTN:  DAMA-CSS-N


Commander                                                    1 copy each
Harry Diamond Laboratories
Department of the Army
2800 Powder Mill Road
Adelphi, MD  20783
    ATTN:  DELHD-N-NP
    ATTN:  DELHD-R J. Rosado
    ATTN:  DELHD-TA-L (Tech. Lib.)


U.S. Army Missile Command
Redstone Scientific Information Center                        3 Copies
Attn:  DRSMI-RPRD (Documents)
Redstone Arsenal, Alabama  35809


Commander                                                    1 copy
U.S. Army Missile Command
Redstone Arsenal, Alabama  35898
    ATTN:  DRCPM-PE-EA


Commander
U.S. Army Nuclear and Chemical Agency
7500 Backlick Road                                           1 copy
Building 2073
Springfield, VA  22150
    ATTN:  Library


Commander                                                    1 Copy
U.S. Army Test and Evaluation Command
Aberdeen Proving Ground, MD  21005
    ATTN:  DRSTE-EL


Commanding Officer                                           1 Copy
Naval Intelligence Support Center
4301 Suitland Road, Bldg. 5
Washington, D.C.  20390
    ATTN:  NISC-45

```
Commander                                              1 Copy
Naval Weapons Center
China Lake, CA  93555
     ATTN:  Code 233 (Tech. Lib.)


Officer in Charge                                      1 copy each
White Oak Laboratory
Naval Surface Weapons Center
Silver Spring, MD  20910
     ATTN:  Code R40
     ATTN:  Code F31


Air Force Weapons Laboratory                           1 copy each
Kirtland AFB, New Mexico  87117
     ATTN:  SUL
     ATTN:  CA
     ATTN:  APL
     ATTN:  Lt. Col. Generosa


Deputy Chief of Staff
Research, Development and Accounting                    1 Copy
Department of the Air Force
Washington, D.C.  20330
     ATTN:  AFRDQSM


Space and Missile Systems Organization/IN              1 Copy
Air Force Systems Command
P. O. Box 92960
Worldway Postal Center
Los Angeles, CA  90009
     ATTN:  IND D. Muskin (Intelligence)


HQ BMO/MM                                              1 Copy
Norton AFB, CA  92409
     ATTN:  Col. J. M. Wells


Space and Missile Systems Organization/SK              1 Copy
Air Force Systems Command
Post Office Box 92960
Worldway Postal Center
Los Angeles, CA  90009
     ATTN:  SKF P. Stadler (Space Comm. Systems)


AVCO Research and Systems Group                        1 Copy
201 Lowell Street
Wilminton, MA  01887
     ATTN:  Library A830
```

BDM Corporation                                          1 Copy
7915 Jones Branch Drive
McLean, Virginia  22101
    ATTN:  Corporate Library


Berkeley Research Associates                             1 Copy
P.O. Box 983
Berkeley, CA  94701
    ATTN:  Dr. Joseph Workman


Berkeley Research Associates                             1 Copy each
P.O. Box 852
5532 Hempstead Way
Springfield, VA  22151
    ATTN:  Dr. Joseph Orens
    ATTN:  Dr. Nino Pereira


Boeing Company                                           1 Copy
P. O. Box 3707
Seattle, WA  98134
    ATTN:  Aerospace Library


The Dikewood Corporation                                 1 Copy
1613 University Bldv., N.E.
Albuquerque, New Mexico  8710
    ATTN:  L. Wayne Davis


EG and G Washington Analytical                           1 Copy
   Services Center, Inc.
P. O. Box 10218
Albuquerque, New Mexico  87114
    ATTN:  Library


General Electric Company                                 1 Copy
Space Division
Valley Forge Space Center
P. O. Box 8555
Philadelphia, PA  19101
    ATTN:  J. Peden


General Electric Company - Tempo                         1 Copy
Center for Advanced Studies
816 State Street
P.O. Drawer QQ
Santa Barbara, CA  93102
    ATTN:  DASIAC

```
Institute for Defense Analyses                          1 Copy
1801 N. Beauregard St.
Alexandria, VA  22311
     ATTN:  Classified Library


IRT Corporation                                         1 Copy
P.O. Box 81087
San Diego, CA  92138
     ATTN:  R. Mertz


JAYCOR                                                  1 Copy
11011 Forreyane Rd.
P.O. Box 85154
San Diego, CA  92138
     ATTN:  E. Wenaas


JAYCOR                                                  1 Copy
205 S. Whiting Street, Suite 500
Alexandria, VA  22304
     ATTN:  R. Sullivan


KAMAN Sciences Corp.                                    1 copy each
P. O. Box 7463
Colorado Springs, CO  80933
     ATTN:  J. Hoffman
     ATTN:  A. Bridges
     ATTN:  D. Bryce
     ATTN:  W. Ware


Lawrence Livermore National Laboratory                 1 copy each
University of California
P.O. Box 808
Livermore, California  94550
     Attn:  DOC CDN for L-153
     Attn:  DOC CDN for L-47 L. Wouters
     Attn:  DOC CDN for Tech. Infor. Dept. Lib.


Lockheed Missiles and Space Co., Inc.                  1 copy each
P. O. Box 504
Sunnyvale, CA  94086
     Attn:  S. Taimlty
     Attn:  J.D. Weisner


Lockheed Missiles and Space Co., Inc.                  1 Copy
3251 Hanover Street
Palo Alto, CA  94304
     Attn:  J. Perez
```

Maxwell Laboratory, Inc.                                      1 Copy each
9244 Balboa Avenue
San Diego, CA  92123
      ATTN:  A. Kolb
      ATTN:  M. Montgomery
      ATTN:  J. Shannon


McDonnell Douglas Corp.                                       1 Copy
5301 Bolsa Avenue
Huntington Beach, CA  92647
      ATTN:  S. Schneider


Mission Research Corp.                                        1 Copy each
P. O. Drawer 719
Santa Barbara, CA  93102
      ATTN:  C. Longmire
      ATTN:  W. Hart


Mission Research Corp.-San Diego                              1 Copy
5434 Ruffin Rd.
San Diego, California  92123
      ATTN:  Victor J. Van Lint


Northrop Corporation                                         1 Copy
Northrop Research and Technology Center
1 Research Park
Palos Verdes Peninsula, CA 90274
      ATTN:  Library


Northrop Corporation                                         1 Copy
Electronic Division
2301 120th Street
Hawthorne, CA  90250
      ATTN:  V. Damarting


Physics International Company                                1 Copy each
2700 Merced Street
San Leandro, CA  94577
      Attm:  C. Stallings
      Attn:  C. Gilman


R and D Associates                                          1 Copy each
P.O. Box 9695
Marina Del Rey, CA  90291
      ATTN:  W. Graham, Jr.
      ATTN:  P. Haas

```
Sandia National Laboratories                        1 copy each
P.O. Box 5800
Albuquerque, New Mexico  87115
    ATTN:  Doc Con For 3141
    ATTN:  D. McDaniel
    ATTN:  P. VanDevender
    ATTN:  K. Matzen, Code 4247


Science Applications, Inc.                          1 copy
P. O. Box 2351
La Jolla, CA  92038
    ATTN:  R. Beyster


Spire Corporation                                   1 copy
P. O. Box D
Bedford, MA  01730
    ATTN:  R. Little


SRI International                                    1 copy
333 Ravenswood Avenue
Menlo Park, CA  94025
    ATTN:  S. Dairiki


S-CUBED                                             1 copy
P. O. Box 1620
La Jolla, CA  92038
    ATTN:  A. Wilson


Texas Tech University                               1 copy
P.O. Box 5404
North College Station
Lubbock, TX  79417
    ATTN:  T. Simpson


TRW Defense and Space Systems Group                 1 Copy
One Space Park
Redondo Beach, CA  90278
    ATTN:  Technical Information Center


Vought Corporation                                  1 Copy
Michigan Division
38111 Van Dyke Road
Sterling Heights, Maine  48077
    ATTN:  Technical Information Center
           (Formerly LTV Aerospace Corp.)
```

Naval Research Laboratory
Plasma Radiation Branch
Washington, D.C.   20375

Code 4720   -   50 Copies
Code 4700   -   26 Copies
Code 2628   -   20 Copies

# END

# FILMED

2-85

# DTIC